ISSN 1028-8546

Volume XVII, Number 4
Section: En
December, 2011

Azerbaijan Journal of Physics

Fizika

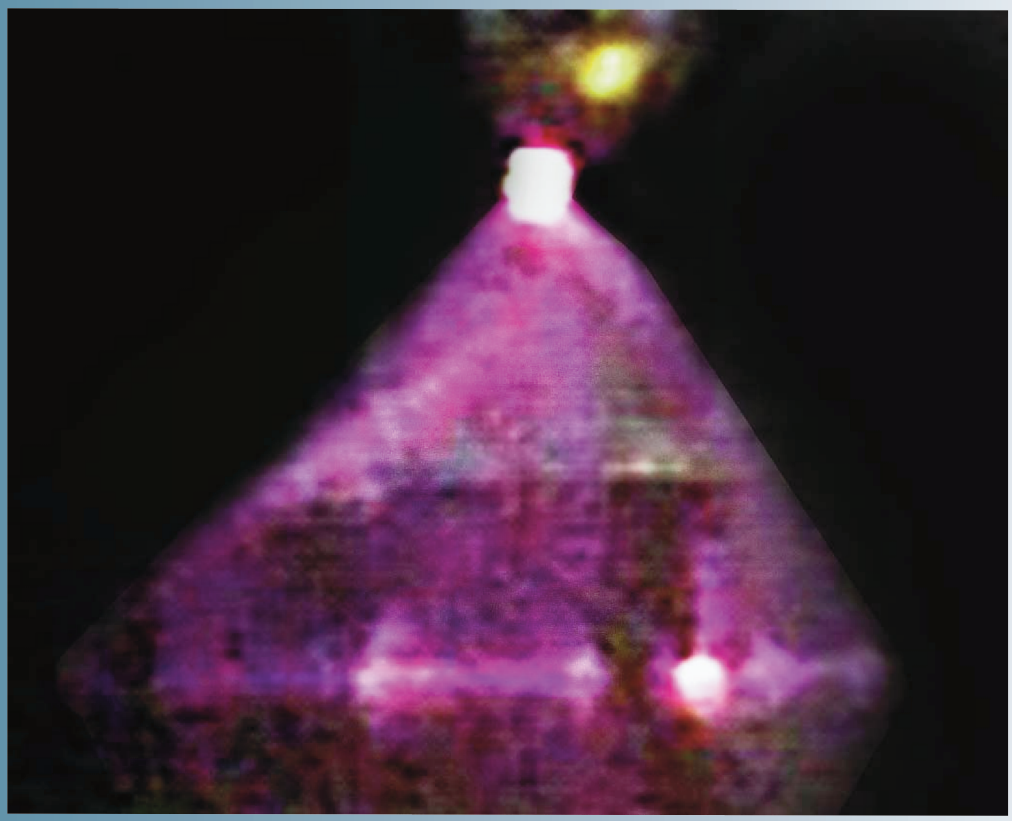

www.physics.gov.az

G.M. Abdullayev Institute of Physics
Azerbaijan National Academy of Sciences
Department of Physical, Mathematical and Technical Sciences

Published from 1995

ISSN 1028-8546
vol. XVII, Number 4, 2011
Section: En

Azerbaijan Journal of Physics

Fizika

G.M.Abdullayev Institute of Physics
Azerbaijan National Academy of Sciences
Department of Physical, Mathematical and Technical Sciences

PUBLISHING OFFICE

33 H.Javid ave, AZ-1143, Baku
ANAS, G.M.Abdullayev Institute of Physics

Tel.: (99412) 439-51-63, 439-32-23
Fax: (99412) 447-04-56
E-mail: jophphysics@gmail.com
Internet: www.physics.gov.az/index1.html

It is authorized for printing: 27.12.2011

Published at: **"ŞƏRQ-QƏRB "**
17 Ashug Alesger str., Baku
Typographer :Aziz Gulaliyev

Sent for printing on: __ 12.2011
Printing approved on: __ 12.2011
Physical binding:_____
Number of copies:_____200
Order:_____

ABOUT THE QUANTIZATION OF ELECTRIC CHARGE IN GAUGE THEORIES

O.B. ABDINOV, F.T. KHALIL-ZADE, S.S. RZAEVA
Institute of Physics of Azerbaijan National Academy of Sciences,
AZ143, Baku, G. Javid av., 33

The theoretical analysis of some gauge models, for the purpose of definition of the conditions for fixing possibility an electric charge in them has been carried. It is shown that presences of the Higgs fields are the necessary condition for quantization of the electric charges in the considered models. The identity of the electric charge quantization conditions coming from as P – invariance of electromagnetic interaction and masses generating Lagrangians as well as the fact of fixation of the fermions fields' hypercharges by the Higgs fields' hypercharges can be interpreted as new properties of the Higgs fields.

Keywords: quantization, gauge theory
PACS: 12.10.Dm; 12.10.-g; 12.15.-y; 14.80.-Bn; 11.15.-q

1. INTRODUCTION

In essence, main task LHC is the comprehensive check and thorough investigation of the basic theoretical tools of modern elementary particles physics - Standard Model (SM) of strong and electroweak interactions. Despite the sometimes unique agreement on the accuracy of the SM predictions with precision experimental data, in the theoretical plan the SM already someone satisfy. Checking the SM in the first place includes not only detection of Higgs boson and investigation of its properties, but also that, perhaps, not less important, establishments of quantitative limits of applicability of SM, i.e. detection and interpretation of those phenomena that cannot be explained within the SM.

In this context, systematic studies such of fundamental characteristics of elementary particles, as the electric charge, the definition and study of the relation of these charges with the properties of Higgs bosons, as well as with other constituent elements of modern models, finding conditions for an unambiguous definition (quantization) of these charges is certainly interesting.

It is known that only massive elementary particles have the electric charges (massless are neutral), so the coupling of electric charge (quantization) with the mechanism of mass generation of elementary particles, it is obvious there is and should be investigated. In this paper, it is accentuated, and this relationship is traced to a number of models of electroweak interactions.

The quantization of electric charge of elementary particles in the SM, in detail discussed in the literature, and has been given a fairly complete answer to this question [1-12].

In the SM the electric charge operator (for the gauge group $SU(2)_L \times U(1)_Y$) is defined in general as $Q = T_3 + \alpha Y$, where T_3 – third projection of the weak isotopic spin operator, Y – hypercharge operator, α — arbitrary parameter. In SM eigenvalues of the weak isotopic spin operator T_3 for elementary particles is strictly defined by non-Abelian gauge symmetry $SU(2)_L$ and doublet structure of left fields. Since the eigenstates of the operator Y in the SM is not determined by the group structure, then to solve the problem of quantization of electric charge in the SM requires two additional conditions which would eliminate the arbitrariness in the choice of the parameter α and the definition of the hypercharge. It is usually assumed that in SM these conditions are, firstly, the requirement of anomaly cancellation [13-15], and, secondly, the gauge-invariant nature of the Yukawa coupling of massive fermions with the SM Higgs boson [1].

Analysis of the quantization of electric charge in some gauge models under these conditions was considered in [1, 2, and 4]. The assumption of electrical neutrality of neutrino the context of SM leads to an explanation of conservation of parity in electromagnetic interactions, and to the quantization of electric charge is considered in [3].

In [9, 10 and 16] it was shown that the eigenstate of the photon and particle charges depend on the hypercharge of the Higgs fields (see also [8]). In addition, it was shown that, in the issue of quantization of electric charge in the SM, it is possible to manage without an explicit accounting of the Higgs mechanism of mass generation, relying instead on the P invariance of the electromagnetic interaction [9, 10, and 16]. This leads to necessity of more detailed investigation of the quantization of electric charge in gauge theories. Thus, the objective of this work – this is a theoretical analysis of a number of models to determine the most general conditions for the possibility of fixation (full definition, quantization) of electric charge in them.

2. ELECTRIC CHARGE QUANTIZATION IN THE SM WITH RIGHT-HANDED NEUTRINO

In [3] it was shown that in gauge models with right-handed neutrino, quantization of electric charge follows from the conditions of anomaly cancellation and nonvanishing fermions masses only if the neutrino is a Majorana particle. As was shown in [5], the introduction of right-handed neutrino into the SM leads to an additional parameter and from the conditions of anomaly cancellation is impossible to obtain the quantization of charge (see also [3]). Note that in all these papers [1 - 8] for the quantization of electric charge used by all the relations following from the conditions of anomaly cancellation with the fixation of the hypercharge of the Higgs field.

It was shown that [11, 12] in the framework of SM in the case of an arbitrary value of the hypercharge of the Higgs field, quantization of the electric charge, is to be independent of the hypercharge of the Higgs doublet.

2.1. SM and hypercharge of left quark doublet. First, consider rather simple possibility of obtaining the relation between the hypercharge of the SM fields [16]. Let us consider SM for the first generation of fermions without mixing and to complete the analysis we assume that the

neutrino has also the right-handed component. In this case we have the following fermions fields

$$\psi_L = \begin{pmatrix} \nu \\ e^- \end{pmatrix}_L, \ \psi_{eR} = e_R, \psi_{\nu R} = \nu_R, \ \psi_{QL} = \begin{pmatrix} u \\ d \end{pmatrix}_L, \ \psi_{uR} = u_R, \ \psi_{dR} = d_R, \tag{1}$$

and Higgs field

$$\varphi = \begin{pmatrix} \varphi^+ \\ \varphi^0 \end{pmatrix} \tag{2}$$

The interaction Lagrangian of the fermions and the Higgs field with gauge fields has the form

$$L = i\overline{\psi}_{fL} \hat{D} \psi_{fL} + i\overline{\psi}_{fR} \hat{D} \psi_{fR} + (D_\mu \varphi)^+ (D_\mu \varphi), \tag{3}$$

where ψ_{fL} – и ψ_{fR} – left and right fermions fields (1), correspondingly and

$$D_\mu = \partial_\mu - ig \frac{\vec{\tau} \vec{A}_\mu}{2} - ig' \frac{X}{2} B_\mu . \tag{4}$$

For the parameters X, causing the interaction of the fields (1) and (2) with the Maxwell field B_μ we choose the following notation

$$\begin{aligned} &X(\varphi) = x_\varphi, \quad X(\psi_L) = x_L \quad X(\psi_{eR}) = x_{eR}, \quad X(\psi_{\nu R}) = x_{\nu R}, \\ &X(\psi_{QL}) = x'_{QL}, \quad X(\psi_{uR}) = x_{uR}, \quad X(\psi_{dR}) = x_{dR}. \end{aligned} \tag{5}$$

We assume that the parameters (5) are real.

Firs consider the third term in (3). Diagonalization of mass matrix of neutral fields leads to

$$\begin{aligned} A_\mu^3 &= A_\mu \sin\theta_\varphi + Z_\mu \cos\theta_\varphi, \\ B_\mu &= A_\mu \cos\theta_\varphi - Z_\mu \sin\theta_\varphi. \end{aligned} \tag{6}$$

where, using notation (5)

$$\sin\theta_\varphi = x_\varphi g' / \bar{g}_\varphi, \quad \cos\theta_\varphi = g / \bar{g}_\varphi, \quad \bar{g}_\varphi = \sqrt{g^2 + x_\varphi^2 g'^2}. \tag{7}$$

The expression for the transformation of the fields A_μ^3 and B_μ to the physical fields A_μ and Z_μ can also be obtained from $i\overline{\psi}_L \hat{D} \psi_L$ and $i\overline{\psi}_{QL} \hat{D} \psi_{QL}$ terms. It is easy to see that from the $i\overline{\psi}_L \hat{D} \psi_L$ term for the mixing angle of neutral fields, we have

$$\sin\theta_L = -\frac{x_L g'}{\sqrt{g^2 + x_L^2 g'^2}}. \tag{8}$$

Mixing angle of neutral fields obtained from the $i\overline{\psi}_{QL} \hat{D} \psi_{QL}$ term, has the form

$$\sin\theta_{QL} = \frac{x'_{QL} g'}{\sqrt{g^2 + x'^2_{QL} g'^2}}. \tag{9}$$

In general, there is no theoretical reason to require the equality of these angles. However, experimental data on the measurement of the Weinberg angle in the purely leptonic, semileptonic and hadronic processes (within experimental error) show the equality of these angles. Thus we have

$$x_\varphi = -x_L, \quad x_\varphi = x'_{QL}, \quad x_L = -x'_{QL}. \tag{10}$$

The expressions (10) show that the parameters X and hence the coupling constants of the Higgs and fermionic fields with the field B_μ equal in absolute value.

In the SM, the quantity defining the interaction of the Higgs and fermionic fields with the field B_μ is the weak hypercharge (hereinafter hypercharge). If the parameters (5) are usual SM hypercharges, we reveal that the hypercharge values of the Higgs and leptonic fields in the SM $(Y_\varphi^{SM} = 1, \ Y_L^{SM} = -1)$ really satisfy the first condition (10). The hypercharge of the left-handed quark field in the SM is equal to $Y_{QL}^{SM} = 1/3$; hence, the second and third conditions (10) are not met. As a result, in general, we find

that the quantity that characterizes the interaction of the left-handed quark field with the filed B_μ (x'_{QL}) cannot be identified with the hypercharge of the left-handed quark field of the SM (Y_{QL}^{SM}). Consequently, it is necessary to interpret the quantity and reveal its relation to the hypercharge. This difficulty of the SM may be overcome by using the following three facts:

- The anomaly cancellation conditions [1–8], from which it follows that $x'_{QL} = 3x_{QL} = 3Y_{QL}^{SM}$;
- The fact of equality of the Weinberg angle measured in purely leptonic, semileptonic and hadronic processes and assume $x'_{QL} = 3x_{QL} = 3Y_{QL}^{SM}$ in order to be consistent with the experiment;
- Assumed that the ratio of hypercharges of the left quark and lepton fields to the hypercharge of the Higgs field are baryon and lepton quantum numbers, respectively [12];

$$\frac{x_{QL}}{x_\varphi} = B, \quad \frac{x_L}{x_\varphi} = -L.$$

However, the model itself and the above listed facts do not allow any interpretation of the quantity (x'_{QL}). The connection of this quantity with the SM hypercharge may be determined only from the relation $x'_{QL} = 3x_{QL} = 3Y_{QL}^{SM}$ which follows from the anomaly cancellation conditions. As will be seen later, this relation is sufficient to have the electric charge quantization in the SM. In this case, the conditions (10) can be written as

$$x_\varphi = -x_L, \quad x_\varphi = 3x_{QL}, \quad x_L = -3x_{QL}, \qquad (11)$$

hence, all the parameters $\boldsymbol{x}$ may be identified with the hypercharge of the SM fields. When the Higgs field is absent in theory, we have only one condition $x_L = -3x_{QL}$. Thus, including the Higgs field into the theory causes the hypercharges of left-handed fermionic fields to be fixed by the hypercharge of the Higgs field.

2.2. Quantization of electric charge. The expression for the charges of the fermions can be obtained from the interaction of leptons and quarks with the electromagnetic field. For such interactions in this case, we have

$$L = L_{l\gamma} + L_{q\gamma},$$

where

$$L_{l\gamma} = \bar{\nu}\gamma_\mu(Q_\nu + Q'_\nu\gamma_5)\nu A_\mu + \bar{e}\gamma_\mu(Q_{0e} + Q'_{0e}\gamma_5)eA_\mu,$$
$$L_{q\gamma} = \bar{u}\gamma_\mu(Q_{1u} + Q'_{1u}\gamma_5)uA_\mu + \bar{d}\gamma_\mu(Q_{2d} + Q'_{2d}\gamma_5)dA_\mu. \qquad (12)$$

Here

$$Q_\nu = \frac{g}{4}\left(1 + \frac{x_L + x_{\nu R}}{x_\varphi}\right)\sin\theta_\varphi, \qquad Q'_\nu = \frac{g}{4}\left(1 + \frac{x_L - x_{\nu R}}{x_\varphi}\right)\sin\theta_\varphi,$$
$$Q_{0e} = -\frac{g}{4}\left(1 - \frac{x_L + x_{eR}}{x_\varphi}\right)\sin\theta_\varphi, \qquad Q'_{0e} = -\frac{g}{4}\left(1 - \frac{x_L - x_{eR}}{x_\varphi}\right)\sin\theta_\varphi. \qquad (13)$$

$$Q_{1u} = \frac{g}{4}\left(1 + \frac{x_{QL} + x_{uR}}{x_\varphi}\right)\sin\theta_\varphi, \qquad Q'_{1u} = \frac{g}{4}\left(1 + \frac{x_{QL} - x_{uR}}{x_\varphi}\right)\sin\theta_\varphi,$$
$$Q_{2d} = -\frac{g}{4}\left(1 - \frac{x_{QL} + x_{dR}}{x_\varphi}\right)\sin\theta_\varphi, \qquad Q'_{2d} = -\frac{g}{4}\left(1 - \frac{x_{QL} - x_{dR}}{x_\varphi}\right)\sin\theta_\varphi. \qquad (14)$$

Undesirable terms in (12) can be eliminated by the requirement of the *P* invariance of electromagnetic interaction [17], which leads to $Q'_\nu = 0$, $Q'_{0e} = 0$, $Q'_{1u} = 0$, and $Q'_{2d} = 0$, whence we get

$$x_L = x_{\nu R} - x_\varphi, x_L = x_{eR} + x_\varphi,$$
$$x_{QL} = x_{uR} - x_\varphi, \quad x_{QL} = x_{dR} - x_\varphi. \qquad (15)$$

We note that relations (15) also follow from the Yukawa interaction Lagrangian

$$L^f_{mass} = f_e\overline{\Psi}_L\Psi_{eR}\varphi + f_\nu\overline{\Psi}_L\Psi_{\nu R}\varphi^c + f_d\overline{\Psi}_{QL}\Psi_{dR}\varphi + f_u\overline{\Psi}_{QL}\Psi_{uR}\varphi^c + h.c., \qquad (16)$$

where $\varphi^c = i\tau_2\varphi^*$.

Moreover in the case when there is no in the model right-handed neutrino, the requirement of P invariance of the electromagnetic interaction and the condition of electrical neutrality of neutrinos are equivalent (see also [3]).

Excluding the hypercharges of right lepton fields in (13) and (14), we have

$$Q_\nu = \frac{Q_e}{2}\left(1+\frac{x_L}{x_\varphi}\right), \quad Q_{0e} = -\frac{Q_e}{2}\left(1-\frac{x_L}{x_\varphi}\right), Q_u = \frac{Q_e}{2}\left(1+\frac{x_{QL}}{x_\varphi}\right), \quad Q_d = -\frac{Q_e}{2}\left(1-\frac{x_{QL}}{x_\varphi}\right), \tag{17}$$

where $Q_e = g\sin\theta_\varphi = x_\varphi g g'/\overline{g}_\varphi$, $\overline{g}_\varphi = \sqrt{g^2 + x_\varphi^2 g'^2}$.

Expressions (17) for the charges of the particles can be regarded as evidence of the quantization of electric charge of leptons and quarks. Taking into account (11) for numerical values of the charges of leptons and quarks (17), we have

$$Q_\nu = 0, \quad Q_{0e} = -Q_e, \quad Q_u = \frac{2}{3}Q_e, \quad Q_d = -\frac{1}{3}Q_e. \tag{18}$$

Similar expressions can be obtained for other families of leptons and quarks. These results define the quantization and numerical values of the electric charge of leptons and quarks.

Thus, we conclude that relations (11) and (15) are necessary conditions for the quantization of electric charge and, hence, without the presence of the Higgs field in this case there is no quantization of electric charge. In this case, the concrete value of the hypercharge of the Higgs boson is not so important. In contrast to the results of [1 – 8] in the model with the right-handed neutrino in the context of solving the problem of quantization of electric charge is not necessary to include into the SM Majorana neutrino. In addition, there is no necessity to use all the relations coming from the conditions of anomaly cancellation and does not require fixation of the hypercharge of any fields. Since in this case, the quantization conditions obtained from the P invariance of the electromagnetic interaction and gauge invariance of the Yukawa interaction (which generates the fermion masses) are identical, in the issue of quantization of electric charge in the SM it is possible to manage and without the obvious account of the Higgs mechanism of generation of mass, relying instead against P invariance of electromagnetic interaction which is caused by identity of charges left and right fermions.

Interaction of the Higgs field with the fermion fields (or the condition of P invariance of electromagnetic interaction) also leads to the fixation of the hypercharges of right fields

$$x_{\nu R} = 0, \quad x_{eR} = -2x_\varphi, \quad x_{dR} = -\frac{2}{3}x_\varphi, \quad x_{uR} = \frac{4}{3}x_\varphi. \tag{19}$$

In this case the expression of charges (17) can be written as

$$\frac{Q_f}{Q_e} = T_{3L}^f + \frac{x_{fL}}{2y_\varphi}. \tag{20}$$

where T_{3L}^f – the third component of isotopic spin, and x_{fL} – left hypercharge fermion field.

Expression (20) coincides in form with the known formula of charge but is a generalization of the derived expressions for the electric charge of a particle. It describes and explains the values of particle charges (in view of the conditions (11)). Expression (20) also follows from the general principles of the gauge invariance of the model under consideration [3, 11].

To conclude this section, we note that the dependence of the conditions of quantization of electric charge from the hypercharge of the Higgs field and the fact of the fixation of hypercharges of fermions fields by Higgs field hypercharge (formula (11), (15), (17)) can be interpreted as having the influence of the Higgs field on the quantization of electric charge.

3. ELECTRIC CHARGE QUANTIZATION IN $SU_C(3)xSU(3)_L xU(1)_X$ MODEL

The models with the gauge $SU_C(3)xSU(3)_L xU(1)_X$ symmetry group have attracted greater interest in recent years in view of the opportunity to solve the problem of generations on the basis of the cancellation of chiral anomalies [18 – 21]. In these 3-3-1 models, progress was made towards the solution to problems such as that of generations [21–23], neutrino mass [24], and the parity violation in atomic transitions [25].

The possibility of quantizing the electric charge using the minimal $SU_C(3)xSU(3)_L xU(1)_X$ (without exotic particles) model and the model with right-handed component of neutrino was studied in [8]. It was shown in this paper that the electric charge quantization does not depend on the classical constraints that follow from the Lagrangian of interaction generating the masses of fermions, is closely allied to the generation number problem and is a natural consequence of the electric charge conservation and of the anomaly cancellation conditions. In contrast to the results of this work we have shown [9,10,16] that the conditions of quantization of electric charge follows from both the P invariance of the electromagnetic interaction and gauge invariance of the Yukawa interaction (which generates the fermion masses) are the same.

In this part of the paper we consider the possibility of quantization of electric charge in the $SU_C(3)xSU(3)_L xU(1)_X$ model with exotic particles that do not depend on the parameters α and β, and investigate the question of the influence of the Higgs fields on the quantization of electric charge.

3.1. The structure of the $SU_C(3)xSU(3)_L xU(1)_X$ *model.* Within the 3-3-1 models electric charge is defined as a linear combination of generators of

$$\hat{Q} = \alpha \hat{T}_3 + \beta \hat{T}_8 + X \hat{I}, \tag{21}$$

Where $T_3 = \frac{1}{2} diag(1,-1,0)$, $T_8 = \frac{1}{2\sqrt{3}} diag(1,1,-2)$ and the normalization is chosen so that $Tr(T_\alpha T_\beta) = \frac{1}{2}\delta_{\alpha\beta}$. Parameters α and β are used to classify the various 3-3-1 models [27].

Hypercharge fermion (and Higgs) fields, causing interaction with the Maxwell field, is defined as

$$\hat{Y} = \beta \hat{T}_8 + X \hat{I}. \tag{22}$$

Note that because the purpose of this part is to study the quantization of electric charge, then the expression as an electric charge (21) and hypercharge fields (22) don't be used later.

Consider the case that symmetry is broken by three Higgs fields with nonzero vacuum averages [16.26].

$$<\chi> = \frac{1}{\sqrt{2}}\begin{pmatrix} 0 \\ 0 \\ V \end{pmatrix}, \quad <\rho> = \frac{1}{\sqrt{2}}\begin{pmatrix} 0 \\ \upsilon \\ 0 \end{pmatrix}, \quad <\eta> = \frac{1}{\sqrt{2}}\begin{pmatrix} u \\ 0 \\ 0 \end{pmatrix}. \tag{23}$$

The Lagrangian describing the interactions of Higgs fields with gauge fields is

$$V_{kin} = (D_\mu \chi)^+ (D_\mu \chi) + (D_\mu \eta)^+ (D_\mu \eta) + (D_\mu \rho)^+ (D_\mu \rho). \tag{24}$$

Hereafter, the quantity D_μ for each field interacting with gauge fields is

$$D_\mu = \partial_\mu - igT_a W_{a\mu} - ig' T_9 X B_\mu, \tag{25}$$

where T_a $(a = 1,...,8)$ are generators of the group $SU(3)_L$ and $T_9 = \frac{1}{\sqrt{6}} diag(1,1,1)$ are chosen so as to satisfy the condition $Tr(T_a T_b) = \frac{1}{2}\delta_{ab}$ $(a,b = 1,2,...,9)$; g and g' are the coupling constants.

Coupling constants (hypercharge) of Higgs fields (23) with a field B_μ denoted as X_χ, X_ρ, X_η, and assume that the vacuum expectation values of Higgs fields satisfy the condition $V >> \upsilon >> u$ (as in [19]).

For lepton and quark fields, we choose the following representation (we consider one family of quarks and leptons without mixing):

$$\psi_{lL} = \begin{pmatrix} \nu \\ e^- \\ N \end{pmatrix}_L \sim (1,3,y_{lL}), \quad \psi_{eR} = e_R \sim (1,1,y_{eR}), \quad \psi_{NR} = N_R \sim (1,1,y_{NR}),$$

$$\psi_{QL} = \begin{pmatrix} u \\ d \\ U \end{pmatrix}_L \sim (3,3,y_{QL}), \quad \psi_{uR} = u_R \sim (3,1,y_{uR}), \tag{26}$$

$$\psi_{dR} = d_R \sim (3,1,y_{dR}), \quad \psi_{UR} = U_R \sim (3,1,y_{UR}).$$

3.2. Quantization of electric charge. In this model, the transformation of neutral fields $W_{3\mu}, W_{8\mu}, B_\mu$ in the physical photon field A_μ is [16.26]:

$$A_\mu = -\frac{g'}{\sqrt{2}\bar{g}}(X_\rho - X_\eta) W_{3\mu} + \frac{3g'}{\sqrt{6}\bar{g}}(X_\rho + X_\eta) W_{8\mu} + \frac{3g'}{\sqrt{6}\bar{g}}(X_\rho + X_\eta) B_\mu, \tag{27}$$

where $\bar{g} = g[3 + 2t^2(X_\eta^2 + X_\rho^2 + X_\eta X_\rho)]^{1/2}$, $t = g'/g$.

From expressions (27), it is clear that the eigenstate of the photon does not contain vacuum averages of the Higgs fields but depends on the hypercharges of the Higgs fields. Moreover, to meet with quantum electrodynamics, based on an unbroken

$U(1)_Q$ gauge group, the photon field must satisfy such general properties of the electromagnetic interaction, as P invariance [17].

Like in Section 2, in this case, undesirable terms in the expression of the interaction of leptons and quarks with the electromagnetic field may be eliminated by involving the P invariance of electromagnetic interaction, which results to the conditions

$$y_{lL} = X_\eta, \qquad y_{eR} = X_\eta - X_\rho, \qquad y_{NR} = X_\eta - X_\chi,$$
$$y_{QL} - y_{uR} = X_\eta, \qquad y_{QL} - y_{dR} = X_\rho, \qquad y_{QL} - y_{UR} = X_\chi. \tag{28}$$

Note that the lepton masses in the considered model are generated by the interaction

$$L^f_{mass} = f_e \overline{\Psi}_{lL} \rho \Psi_{eR} + f_N \overline{\Psi}_{lL} \chi \Psi_{NR} + f_u \overline{\Psi}_{QL} \eta \Psi_{uR} + f_d \overline{\Psi}_{QL} \rho \Psi_{dR} + f_U \overline{\Psi}_{QL} \chi \Psi_{UR} + h.c., \tag{29}$$

from which, we also get the second and third conditions (28).

Consequently, like in Section 1 we obtained that the condition of quantization of electric charge follows from both the P invariance of the electromagnetic interaction and gauge invariance of the Yukawa interaction are identical. It should also be noted that, when the right-handed component of the neutrino is absent in the model, the conditions of the electromagnetic interaction *P* invariance and of the electrical neutrality of the neutrino are equivalent.

For the electric charges of leptons and quarks in this case we have

$$Q_\nu = 0, \qquad Q_N = -Q_e \frac{2X_\eta + X_\rho}{X_\eta - X_\rho},$$
$$Q_u = Q_e \frac{X_\eta - y_{QL}}{X_\eta - X_\rho}, \quad Q_d = Q_e \frac{X_\rho - y_{QL}}{X_\eta - X_\rho}, \quad Q_U = Q_e \frac{X_\chi - y_{QL}}{X_\eta - X_\rho}, \tag{30}$$

where

$$Q_e = \frac{gg'}{\sqrt{2}\overline{g}}(X_\eta - X_\rho) \tag{31}$$

The expressions (30) may be interpreted as evidence for the quantization of the electric charge of leptons and quarks. These expressions do not, however, determine the numerical values (in units of the electron charge) of the electric charges of the *N* – lepton and quarks.

Note that, unlike the simple case discussed in Section 1, the gauge models with extra Higgs fields and with an extended symmetry group do not allow relations (similar to the relations (11)) connecting the hypercharges of Higgs and fermionic fields. In such models, additional relations can be derived from the cancellation conditions of gauge [13, 14] and gauge-gravitational anomalies [15]. In the considered model, the conditions for the cancellation of triangular anomalies result in the following relations [16, 26]:

$$y_{lL} = X_\eta, \quad y_{eR} = 2X_\eta, \quad y_{NR} = X_\chi,$$
$$y_{QL} = -\frac{1}{3}X_\eta, \quad y_{uR} = -\frac{4}{3}X_\eta, \quad y_{dR} = \frac{2}{3}X_\eta, \quad y_{UR} = -\frac{1}{3}X_\eta. \tag{32}$$

In view of (32) and (30), we find

$$Q_\nu = 0, \quad Q_e = \frac{\sqrt{2}gg'X_\eta}{(3 + 2X_\eta^2 t^2)^{1/2}}, \quad Q_N = -\frac{1}{2}Q_e, Q_u = \frac{2}{3}Q_e, \quad Q_d = -\frac{1}{3}Q_e, \quad Q_U = \frac{1}{6}Q_e. \tag{33}$$

Expressions similar to (33) can be deduced for other families of leptons and quarks as well. These results define the quantization and numerical values of the electric charge of leptons and quarks (in terms of the electron charge).

Conditions (28) and the relations following from the conditions for the cancellations of triangular anomalies (32) fix the hypercharges of all fields and can be interpreted as having the influence of the Higgs fields on the quantization of electric charge. Thus, if there are no conditions (28) and (32), there is no quantization of the electric charge; hence, in the considered model, these conditions are conditions for the quantization of the electric charge of particles. It should also be noted that, and in this case, the issue of quantization of electric charge, can do without an explicit account of the Higgs mechanism of mass generation, relying instead on the P invariance of electromagnetic interaction.

4. ELECTRIC CHARGE QUANTIZATION IN $SU_C(3)xSU(3)_L\,xU(1)_X\,xU^{'}(1)$ MODEL

In this subsection of the paper, using the $SU_C(3)xSU(3)_L\,xU(1)_X\,xU^{'}(1)$ model discussed in [16, 28], we shall examine the influence of Higgs fields on the quantization of the electric charge of particles. Note that the $SU_C(3)xSU(3)_L\,xU(1)_X\,xU^{'}(1)$ model has the following fermionic and Higgs fields:

$$\psi_{lL}=\begin{pmatrix}\nu\\ e\\ N\end{pmatrix}_L\sim(1,3,y_{lL},y^{'}_{lL}),\psi_{eR}=e_R\sim(1,1,y_{eR},y^{'}_{eR}),\psi_{NR}=N_R\sim(1,1,y_{NR},y^{'}_{NR}),$$

$$\psi_{QL}=\begin{pmatrix}u\\ d\\ U\end{pmatrix}_L\sim(3,3,y_{QL},y^{'}_{QL}),\psi_{uR}=u_R\sim(1,1,y_{uR},y^{'}_{uR}),\ \psi_{dR}=d_R\sim(3,1,y_{dR},y^{'}_{dR}),\psi_{UR}=U_R\sim(3,1,y_{UR},y^{'}_{UR}),$$

$$<\chi>=\frac{1}{\sqrt{2}}\begin{pmatrix}0\\ 0\\ V\end{pmatrix}\sim(1,3,X_\chi,X^{'}_\chi),<\rho>=\frac{1}{\sqrt{2}}\begin{pmatrix}0\\ \upsilon\\ 0\end{pmatrix}\sim(1,3,X_\rho,X^{'}_\rho),<\eta>=\frac{1}{\sqrt{2}}\begin{pmatrix}u\\ 0\\ 0\end{pmatrix}\sim(1,3,X_\eta,X^{'}_\eta).$$

In this model, the photon field A_μ is a linear combination of the fields $W_{3\mu},W_{8\mu},B_\mu,C_\mu$

$$A_\mu=\frac{tt^{'}}{\bar{t}}W_{3\mu}+\frac{\sqrt{3}tt^{'}}{\bar{t}}W_{8\mu}+\frac{\sqrt{6}t}{\bar{t}}B_\mu-\frac{\sqrt{6}t^{'}}{\bar{t}}C_\mu,\qquad(34)$$

where we used the notation:

$$\bar{t}=\sqrt{t^2t'^2(P^2+3P_1^2)+6t'^2P_2^2+6t^2P_3^2}\ ;P=X_\chi(X^{'}_\eta-X')-X^{'}_\chi(X_\eta-X_\rho)+2(X_\rho X^{'}_\eta-X_\eta X^{'}_\rho);$$
$$P_1=X_\chi(X^{'}_\eta+X^{'}_\rho)-X^{'}_\chi(X_\eta+X_\rho);\ P_2=X^{'}_\chi+X^{'}_\rho+X^{'}_\eta;\ P_3=X_\chi+X_\rho+X_\eta,\qquad(35)$$

here $X_\chi,X_\eta,X_\rho,X^{'}_\chi,X^{'}_\eta,X^{'}_\rho-U(1)$ and $U'(1)$ hypercharges of Higgs fields, correspondingly, $t=g^{'}/g,t^{'}=g^{''}/g$ and $g,g^{'},g^{''}$ – coupling constants.

Like in Sections 2 and 3, it follows from expressions (34) and (35) that the eigenstate of the photon does not contain vacuum averages of the Higgs fields but depends on Higgs fields' hypercharges.

Taking into account that the electromagnetic interaction is *P* invariant for the electric charges of leptons and quarks in this case we have [16, 28]

$$Q_\nu=0,\quad Q_e=gtt^{'}P/\bar{t},\quad Q_N=-\frac{3P_1+P}{2P}Q_e,$$
$$Q_u=\frac{P+P_1+2(P_2y_{QL}-P_3y^{'}_{QL})}{2P}Q_e,Q_d=-\frac{P-P_1-2(P_2y_{QL}-P_3y^{'}_{QL})}{2P}Q_e,\qquad(36)$$
$$Q_U=-\frac{P_1-P_2y_{QL}+P_3y^{'}_{QL}}{P}Q_e.$$

Note that, like in Sections 2, 3 and in this case when the neutrino right-handed component absent, the requirement of the *P* invariance of electromagnetic interaction and the condition of the zero neutrino charge are equivalent in the model under consideration, as well. We also present some relations connecting the hypercharges of Higgs and lepton fields that follow from the electromagnetic interaction *P* invariance:

$$P+P_1+2y_{lL}P_2-2y^{'}_{lL}P_3=0,\ -P+P_1+2(y_{lL}-y_{eR})P_2-2(y^{'}_{lL}-y^{'}_{eR})P_3=0,$$
$$-P_1+(y_{lL}-y_{NR})P_2-(y^{'}_{lL}-y^{'}_{NR})P_3=0,\ P_2y_{uR}-P_3y^{'}_{uR}=P_2y_{QL}-P_3y^{'}_{QL}+\frac{1}{2}(P+P_1),$$
$$P_2y_{dR}-P_3y^{'}_{dR}=P_2y_{QL}-P_3y^{'}_{QL}-\frac{1}{2}(P-P_1),\ P_2y_{UR}-P_3y^{'}_{UR}=P_2y_{QL}-P_3y^{'}_{QL}-P.\qquad(37)$$

Note that, from the conservation of the sum of $U(1)$ and $U^{'}(1)$, hypercharges in the Lagrangian

$$L_Y = f_e\overline{\psi}_{lL}\rho\psi_{eR} + f_N\overline{\psi}_{lL}\chi\psi_{NR} + f_u\overline{\psi}_{QL}\eta\psi_{uR} + f_d\overline{\psi}_{QL}\rho\psi_{dR} + f_U\overline{\psi}_{QL}\chi\psi_{UR} + h.c, \tag{38}$$

which generates the masses of leptons, we get:

$$\begin{aligned} &y_{lL} + y'_{lL} = y_{eR} + y'_{eR} + X_\rho + X'_\rho, \quad y_{lL} + y'_{lL} = y_{NR} + y'_{NR} + X_\chi + X'_\chi, \\ &y_{QL} + y'_{QL} - y_{uR} - y'_{uR} = X_\eta + X'_\eta, \quad y_{QL} + y'_{QL} - y_{dR} - y'_{dR} = X_\rho + X'_\rho, \\ &y_{QL} + y'_{QL} - y_{UR} - y'_{UR} = X_\chi + X'_\chi, \end{aligned} \tag{39}$$

which, as is easily verified, leads to relations (37). Hence, in this case the conditions of the *P* invariance of the electromagnetic interaction of leptons are also identical to the condition of gauge invariance of the Yukawa interaction.

The expressions (36) may be treated as evidence for the quantization of the electric charge of leptons and quarks, while Eq. (37) (or (39)) are the conditions for the quantization of the electric charge of leptons and quarks. Expressions (36) which are dependent on the hypercharges of Higgs fields, do not determine the numerical values of the particle charges (in terms of electron charge). Note that, in the considered model, like in Section 2, it is impossible to derive additional relations (similar to relations (11)) connecting the hypercharges of the Higgs and fermionic fields. Additional relations can be deduced from the anomaly cancellation conditions, which in our case look like [16, 28]:

$$\begin{aligned} &y_{lL} + y'_{lL} = X_\eta + X'_\eta, \quad y_{eR} + y'_{eR} = 2(X_\eta + X'_\eta), \quad y_{NR} + y'_{NR} = X_\eta + X'_\eta, \\ &y_{QL} + y'_{QL} = -\frac{1}{3}(X_\eta + X'_\eta), \quad y_{dR} + y'_{dR} = \frac{2}{3}(X_\eta + X'_\eta), \\ &y_{uR} + y'_{uR} = -\frac{4}{3}(X_\eta + X'_\eta), \quad y_{UR} + y'_{UR} = -\frac{1}{3}(X_\eta + X'_\eta). \end{aligned} \tag{40}$$

Considering (40) in (36), for the electric charges of leptons and quarks in the considered model, we have:

$$Q_\nu = 0, \quad Q_N = -\frac{1}{2}Q_e, \quad Q_u = \frac{2}{3}Q_e, \quad Q_d = -\frac{1}{3}Q_e, \quad Q_U = \frac{1}{6}Q_e. \tag{41}$$

5. CONCLUSIONS

As a result of the analysis we can conclude that in these models eigenstate of the photon field depends on the hypercharge of the Higgs fields [8 -10.16]. This in turn leads to the dependence obtained in this paper, the quantization conditions ((15) (19), (28), (32) and (40)) and electric charges of particles ((17), (30), (31) and (36)) from the hypercharge of the Higgs fields. Obviously, if no such conditions, there is no quantization of electric charge of particles, because without these conditions cannot solve the equations that follow from the conditions of anomaly cancellation.

The fixing of the hypercharges of the fermionic fields by the Higgs fields and the dependence of the electric charge quantization conditions on the hypercharges of the Higgs fields point to the necessity of the presence of Higgs fields in the quantization of the electric charge of particles in the considered models. Sufficient conditions are the conditions of anomaly cancellation.

Moreover, contrary to the result of [10], we show that the conditions of electric charge quantization, both those following from the *P* invariance of the electromagnetic interaction and those available in the Lagrangians generating fermion masses, are identical [11, 12, 18]. Hence, in the issue of quantization of electric charge, in considered models, it is possible to manage and without the obvious account of the Higgs mechanism of generation of mass, relying instead against P invariance of electromagnetic interaction which is caused by identity of charges left and right fermions.

In general, in the SM, the electric charge can be quantized and fixed by using only one relation, which follows from the anomaly cancellation conditions, and without fixing the hypercharge of some fields. In this case, introducing the neutrino right-handed component into the model does not give rise to an additional parameter in the conditions of anomaly cancellation, so in the content of electric charge quantization there is no need to enter the Majorana neutrino into the theory.

In considered models the conditions of P invariance of the electromagnetic interaction and gauge invariance of the Yukawa interaction (which generates the fermion masses) are identical [11, 12 and 18]. This fact leads us to consider Higgs fields as a possible mechanism explaining the *P* parity in electromagnetic interactions.

The dependence of the quantization conditions and electric charges of particles from the hypercharge of the Higgs fields, the identity of electric charge quantization conditions, following from Lagrangians generating particle masses and from the P invariance of the electromagnetic interaction and the fact of the fixing of fermionic field hypercharges by the Higgs fields can be interpreted as new properties of Higgs fields. These properties of the Higgs fields demand the account and additional attention at the analysis and interpretation of experimental data.

The work supported by the Fund of Development of the Science under the President of the Azerbaijan Republic (grant EIF-2010-1(1)-40/03-M-5).

[1] *X.-G. He, G.C. Joshi, H. Lew, B.H. McKellar, R.R. Volkas*. 1989 Phys. Rev. D40 3140
[2] *K.S. Babu, R.N. Mohapatra.* 1989 Phys. Rev. Let. 63 938
[3] *K.S. Babu, R.N. Mohapatra*. 1990 Phys. Rev. D42 3866
[4] *R. Foot, H. Lew, G. Joshi, R. R. Volkas.* 1990 Mod. Phys. Let. A5 95
[5] *C. Geng*. 1990 Phys. Rev. D41 1292
[6] *S. Rudaz*. 1990 Phys. Rev. D41 2619
[7] *E. Golwich, P.B. Pal.* 1990 Phys. Rev. D41 3537
[8] *P.V. Dong, H. N. Long.* 2005 hep – ph/0507155v1
[9] *O.B. Abdinov, F.T. Khalil-zade, S.S. Rzaeva.* 2008 hep – ph/0807.4359v1
[10] *O.B. Abdinov, F.T. Khalil-zade, S.S. Rzaeva.* 2009 Fizika, XV, №2, 76
[11] *A. Abbas.* 1990 J. Phys. G: Nucl. Part. Phys., 16 L163
[12] *A. Abbas.* 1990 Phys. Let. B238 344
[13] *S.L. Adler*. 1968 Phys. Rev. 177.2426; *J. S. Bell, R. Jackiw*. 1969 Nuovo Cimento 60A 69; *S.L. Adler, W. Bardeen*. 1969 Phys. Rev. 182 1517
[14] *C. Bouchiat,* J. Iliopoulos, Ph. Meyer. 1972 Phys. Let. B 38 519; *H. Georgi, S. L. Glashow*. 1974 Phys. Rev. D 9 416*; D. Gross, R. Jackiv*. 1972 Phys. Rev. D 6 477
[15] *R. Delbourgo, A. Salam*. 1972 Phys. Let. B40 381; *T. Eguchi, P. Freund.* 1976 Phys. Rev. Let. 37 1251; *L. Alvares-Gaume, E. Witten.* 1983 Nucl. Phys. B234 269
[16] *O.B. Abdinov, F.T. Khalil-zade, S.S. Rzaeva*. Pis'ma v Zhurnal Fizika Elementarnykh Chastits i Atomnogo Yadra, 2010 No. 5 161; O*.B. Abdinov, F.T. Khalil-zade, S.S. Rzaeva* 2010 Physics of Particles and Nuclei Letters, 7 No. 5, pp. 314–325
[17] *T.D. Lee, C.N. Yang*. 1956 Phys. Rev. 104 254; *A. Salam*. Nuovo Cimento.1966 3 837; *V. Kobzarev, L. Okun, I. Pomeranchuk*.1966 Sov. J. Nucl. Phys. 3 837
[18] *F. Pisano and V. Pleitez*.1992 Phys. Rev. D46 410; *P. H. Frampton*, 1992 Phys. Rev. Let. 69 2889; *R. Foot et al*, 1993 Phys. Rev. D47 4158
[19] *M. Singer, J. W. F. Valle, J. Schechter*. 1980 Phys. Rev. D22 738; *R. Foot, H.N. Long, Tuan A. Tran.* 1994 Phys. Rev. D50 34; *J.C. Montero, F. Pisano, V. Pleitez*, 1993 Phys. Rev. D47 2918, 1996 Phys. Rev. D54 4691
[20] *H.N. Long*, 1996 Phys. Rev. D53 437
[21] *W.A. Ponce, D. A. Gutierrez, L.A. Sanchez.* 2004 Phys. Rev. D 69 055007; *A.G. Dias, V. Pleitez*, 2004 Phys. Rev. D 69 077702
[22] *W.A. Ponce, D.A. Gutierrez, L.A. Sanchez*. 2004 hep – ph/031243v3
[23] *W.A. Ponce, J.B. Flores, L.A. Sanchez*. 2001 hep – ph/0103100v2
[24] *H.N. Long*. 1996 hep – ph /9603258v1; 1995 hep – ph/9504274v2
[25] *P.V. Dong, H.N. Long, D.T. Nhung*. 2006 hep – ph /0604199v2
[26] *O.B. Abdinov, F.T. Khalil-zade, S.S. Rzaeva*. 2010 hep-ph/1001.2679 *O.B. Abdinov, F.T. Khalil-zade, S. S. Rzaeva*. 2010 Fizika, XV, №2, p.78
[27] *R.A. Diaz, R.A. Martinez, F. Ochoa.* 2004 hep – ph/0309280v2
[28] *O.B. Abdinov, F.T. Khalil-zade, S.S. Rzaeva*. 2009 Fizika, XV, №1, p.24

Received: 11.10.2011

LIGHT MAGNETOABSORPTION IN QUANTUM RINGS OF FINITE WIDTH

G.B. IBRAGIMOV, R.G. ABBASZADE
H.M.Abdullayev Institute of Physics of Azerbaijan NAS
H. Javid ave., 33, Baku, Azerbaijan, Az 1143

In this paper we study optical transitions of 2D electrons in a ring with Volcano confinement potential in a uniform magnetic field. The absorption coefficient has been calculated in the case of a nondegenerate electron gas.

Keywords: magnetoabsorption, Volkano ring, absorption coefficient, optical transition
PACS: 78. 20. Ls

The successes of modern nanostructure technology allow us to create the systems of enough complex geometric form. So-called quantum rings obtained on the basis of heterostructures [1,2] in which two-dimension electron gas forms, are character examples.

For description of ring electron properties are used the different models. In particular, the model of two- and three-dimension wire with periodic boundary conditions [3-6] can be related to simplest models of the rings. The more complex models for the description of ring confinement, such as Hill coefficient and Volcano potential [7,8] are also used. The potential in Volcano model is successful used for the explanation of beating in Aronov-Bom oscillations, which are experimentally observed in two-dimension semiconductor ring [9]. In such rings the electron motion along one direction (Oz axis) perpendicular to the plane of the ring own, "is frozen" in the main state by strong surface potential, as the ring width is much less than its internal and external radiuses. That's the two-dimension gas forms in ring plane. The use of such ring models in theoretical investigations is caused by the fact that they allow us to obtain the simple analytical expressions for electron spectrum of the rings at the presence of external magnetic field.

The investigations of optic transitions of 2D-electrons in the ring of Volcano confinement potential being in homogeneous magnetic field are the aim of the given work. Note that investigation of optical transitions is the powerful definition method of energy spectrum parameters and Fermi electron surface [10-12].

We consider the free electron in two-dimension ring which is described by Volcano radial potential [7]:

$$V(r) = \frac{a_1}{r^2} + a_2 r^2 \qquad (1)$$

Here r is particle radius-vector in polar coordinate system, a_1, a_2 are some parameters. The potential (1) allows us to obtained the analytical solution of Schrödinger equation in magnetic field, by other hand, allows us to model the finite width ring.

The expansion energy (1) near minimum

$$V(r_0) = min(V(r))$$

gives as follows

$$V(r) \cong \frac{m^* \omega_0^2}{2}(r - r_0)^2 - V_0 \qquad (2)$$

where:

$$V_0 = 2\sqrt{a_1 a_2}\,,\ \omega_0 = \sqrt{8a_2/m^*}\,,\ r_0 = (a_1/a_2)^{1/4}$$

m^* is particle effective mass. Then electron Hamiltonian in potential (1) and homogeneous magnetic field $B = (0,0,B)$ (Z axis is perpendicular to ring plane) is as follows:

$$\hat{H}_e = -\frac{\hbar^2}{2\dot{m}^*}\left[\frac{1}{r}\frac{\partial}{\partial r}\left(r\frac{\partial}{\partial r}\right) + \frac{1}{r^2}\left(\frac{\partial^2}{\partial \varphi^2}\right)\right] - i\frac{\hbar\omega_c}{2}\frac{\partial}{\partial \varphi} + \frac{m^*\omega_c^2 r^2}{8} + \frac{a_1}{r^2} + a_2 r^2 - V_0 \qquad (3)$$

$\omega_c = eB/m^*c$ is electron cyclotron frequency. The solution of Schrödinger equation for lateral electron motion will be written in the following form [7]:

$$E_{n,m} = \left(n + \frac{1}{2} + \frac{M}{2}\right)\hbar\omega_e - \frac{l_e}{2}\hbar\omega_c - \frac{m^*}{4}\omega_0^2 r_0^2 \qquad (4)$$

$$n = 0,1,2,\ldots \quad l_e = \ldots,-1,0,1,\ldots,$$

$$\Psi_{n,l_e}(r,\varphi)=\frac{1}{\lambda}\left(\frac{\Gamma(n+M+1)}{2^{M+1}n!\,[\Gamma(M+1)]^2\pi}\right)^{1/2} e^{-il_e\varphi}e^{-(1/4)(r/\lambda)^2}\left(\frac{r}{\lambda}\right)^M \times$$
$$\times {}_1F_1\left[-n,M+1,\frac{1}{2}(r/\lambda)^2\right] \qquad (5)$$

Here : $\omega_e=\sqrt{\omega_c^2+\omega_0^2}$, $\lambda=\sqrt{\frac{\hbar}{m^*\omega_e}}$, $M=\sqrt{l_e^2+\frac{2a_1m^*}{\hbar^2}}$

One can find the wave functions and hole spectrum analogously. In further calculations we will consider r_0 and ω_0 parameters similar to electrons and holes for the simplicity and the difference between electron and hole occurs from different values of effective masses of particles and signs of their charge.

The absorption coefficient is described by the following expression [13] in the case of nondegenerate gas in first order of perturbation theory on constant of electron-phonon interaction:

$$\alpha=\frac{2\pi\sqrt{\varepsilon(\omega)}}{c\hbar N_f}\left[1-exp\left(-\frac{\hbar\omega}{kT}\right)\right]\times$$
$$\sum_{nl_e}\sum_{n'l'_e} f_0(E_{nl_e})\left|\left\langle nl_e\left|H_R\right|n'l'_e\right\rangle\right|^2\delta(E_{nl_e}-E_{n'l'_e}+\hbar\omega) \qquad (6)$$

where : $\varepsilon(\omega)$ is real part of dielectric constant, f is photon wave vector, $f_0(E_{n,l_e})$ is electron distribution function, multiplier $\left[1-\exp\left(-\frac{\hbar\omega}{kT}\right)\right]$ takes into consideration the stimulated photon emission.

The operator of electron-photon interaction has the form:

$$H_R=\frac{e}{m^*}\sqrt{\frac{2\pi\hbar N_k}{\varepsilon(\omega)\omega}}\boldsymbol{e_k}\left(p+\frac{e}{c}\boldsymbol{A}\right)$$

where: A is vector potential of homogeneous magnetic field, $\mathrm{e_k}$ is photon polarization vector.

The normalizing constant of distribution function in (6) is found from the condition:

$$\sum_{l_e}\sum_{n} f_0(E_{nl_e})=N$$

Here N is electron number in volume unit.

[1] *A.Fuhrer, S.Luscher, T.Ihn, T.Heinzel, K.Ensslin, W.Wegscheider, M.Bichler*. Nature 413, 822 (2001).

[2] *U.Keyser, S.Borck, R.Haug, M.Bichler, G.Abstreiter, W.Wegscheider,* Semicond. Sci.Technol. 17, 122 (2002).

[3] *A.Schmid* . Phys. Rev. Lett. 66, 80 (1991).

[4] *A.Kopiets*. Phys. Rev. Lett. 70, 3123 (1993).

[5] *D.Loss.* Phys. Rev. Lett. 69, 343 (1993).

[6] *V.A.Margulis, A.V.Shorokhov, H.P.Trushin.* Physica E 10, 518 (2001).

[7] *W.C. Tan, J.C.Inkson*. Phys. Rev. B 60, pp.5626-5638(1999).

[8] *W.-C. Tan, J.C.Inkson*. Phys. Rev. B 53, pp.6947-6950 (1996).

[9] *J.Liu, W.X.Gao, K.Ismail, K.Y.Lee, J.M.Hong, S.Washburn*. Phys. Rev. B 48, 15148 (1993).

[10] *L.Brey, N.F.Johnson, B.I. Halperin* Phys. Rev. B 40, 10647 (1989).

[11] *V.A. Geyler, V.A. Margulis, A.V. Shorokhov* Phys. Rev. B 63, 245316 (2001).

[12] *V.Ya. Demikhovskiy, A.A. Perov*. JETF, 114, 1795 (1998).

[13] *F.G. Bass, I.B. Levinson*. JETF 49, 914 (1970).

Received:18.10.2011

THERMODYNAMIC PARAMETERS OF SOLID SOLUTIONS OF $NiFe_2O_4$ -$ZnFe_2O_4$ SYSTEM

A.H. HABIBZADE, S.I. ALIYEVA, Sh.N. ALIYEVA, T.R. MEKHTIYEV
G.M. Abdullayev Institute of Physics of ANAS
H. Javid ave., 33, AZ-1143, Baku, Azerbaijan

The thermodynamic properties and their temperature dependences in the interval from 300C° up to 1100C° for $Ni_xZn_{1-x}Fe_2O_4$ solid solutions at x = 0, 0.25, 0.5, 0.75, 1.0 are studied.

Keywords: thermodynamic properties, zinc-nickel ferrites.
PACS: 75.10. ± b, 75.30.Ds, 75.40.Cx

The wide application of solid solutions of $NiFe_2O_4$-$ZnFe_2O_4$ system is connected with of their magnetic property peculiarities [1-19]. The technology of $Ni_xZn_{1-x}Fe_2O_4$ micro-powder synthesis is paid a big attention. There are no data on thermodynamic parameters of these poweders .

In the given paper the solid solutions $Ni_xZn_{1-x}Fe_2O_4$ are synthesized by technology in which the co-precipitation process of the corresponding amorphous hydroxides with the further hydrothermal gel treatment by ammonia is used. The choice of the given technology is connected with its simplicity, and also with possibilities of disperse product morphology control because of parameter variety of process carrying out (temperature, solution concentration, process duration and etc). In spite of method simplicity, this chosen synthesis type allows us to obtain the mono-disperse nano-powders in which the particle size is nano-meter units.

The control of the obtained materials is carried out by X-ray and electron-microscopic investigations, earlier published in [19-20].

The investigation results of existence conditions in $NiFe_2O_4$ -$ZnFe_2O_4$ solid solution system and their thermodynamic parameters are presented in the given paper.

The temperature dependence of solubility limit of ferrite components and spinodal curves (in two-phase region, in which the homogeneous ferrite solution is inconstant) are defined from the calculations of mixing free energy for two-component (pseudo-binary) A-B composition at T temperature within framework of ideal solution model [1].

The free energy is defined by the following expression:

$$\Delta G_{mix} = RT(X_A \ln X_A + X_B \ln X_B) + \Omega X_A X_B$$

where A and B are ferrite components; Ω is solubility parameter; X_A and X_B are mole parts of A and B components correspondingly. The mole part is defined by classic expression $X_j = \frac{n_j}{\sum_f n_f}$ where j – A, B; n_f is f substance quantity containing in the solution.

The composition of initial ferrite is well seen on the spinodal and bimodal (fig1) (solubility curve, co-existence curve). The solubility interval is obtained from the condition when first derivative of free energy is equal to zero meanwhile the temperature dependence of component composition (spinodal curve) from condition when secondary one is equal to zero :

$$\left.\begin{aligned} \frac{\partial \Delta G_{mix}}{\partial X_B} = 0; \quad \Omega(2X_B - 1) = RT \ln\left(\frac{X_B}{X_B - 1}\right) \\ \frac{\partial^2 \Delta G_{mix}}{\partial X_B^2} = 0; \quad 2\Omega X_B(1 - X_B) = RT \end{aligned}\right\}$$

The solubility upper critical point corresponds to temperature 960°C. As it is known, the first and second derivatives of chemical potential are equal to zero in critical point, and the third one is positive, i.e. the curve of chemical potential dependence endures the bend in this point.

As the equality of chemical potentials is the co-existence curve equality, so it separates the region of stable solutions from metastable region meanwhile the spinodal is the boundary of absolute instability system.

The presence of metastable and instable regions predetermines the possibility of two mechanisms of system decomposition: nucleofilic or embryonic (between co-existence curve and spinodal) and spinodal (inside the spinodal) ones.

The decay of metastable system at nucleation is carried out in the result of concentration fluctuation formation, the composition of which is close to ones of co-existing phases in balance and the dimension exceeds the critic one. The germ critic dimension decreases with the increase of deeping degree in the metastable region. The germs on the further stages increase because of component diffusion from matrix unbalance solution. The germs with dimensions less than critic value resolve. The system is two-phase one with clear interface on any decay stage.

At spinodal decay the formation of new phases is carried out because of any fluctuations not necessary achieved the critic dimension. In this case the fluctuation amplitude increases, but not their linear dimension, i.e. concentration deviation value from initial one. The decay ends as in the case of nucleation by the formation of two balanced phases.

As $NiFe_2O_4$ -$ZnFe_2O_4$ system is annealed in the high temperature interval up to solid solution in the solubility interval and temperatures of particle germ-formation, so indirect decomposition of stoichiometric ferrite in Ni0 and Zn-ferrites is carried out below the spinodal curve, as it is seen on fig.1. The interdiffusion coefficient between formatting ferrites [2] can be defined also by the formula:

$$\widetilde{D} = (X_A D_A^* + X_B D_B^*)\left(1 + \frac{\partial ln\gamma_A}{\partial lnX_A}\right) = (X_A D_A^* + X_B D_B^*)\left(1 - \frac{4T_c}{T} X_A X_B\right)$$

where D_A^* and D_B^* are interdiffusion coefficients and γ_A, γ_B are corresponding activities. The heats of formation, entropy and Gibbs energy for ferrite components $Ni_xZn_{1-x}Fe_2O_4$ at temperature 298K and normal pressure, and also temperature dependences of these thermodynamic parameters calculated on relations:

$$C_p = A_1 + A_2 T + A_3 T^{-2} + A_4 T^{-0.5} + A_5 T^2$$

$$\frac{(G_T^0 - H_{298}^0)}{T} = \frac{(H_T^0 - H_{298}^0)}{T} - S_T^0$$

$$\Delta_f H_T^0 = \Delta_f H_{298}^0 + \Delta(H_T^0 - H_{298}^0)$$

$$\Delta_f G_T^0 = \Delta_f H_{298}^0 + T\Delta\left(\frac{H_T^0 - H_{298}^0}{T}\right);\ \Delta_f G_T^0 = A + BT + CT^{-2}$$

$$\log K_{f,T} = \frac{\Delta_f G_T^0}{2.30258RT} = \frac{\Delta_f G_{298}^0}{19.145T}$$

where $K_{f,T}$ is equilibrium constant at T temperature, S_T^0 is entropy at temperature T, $(H_T^0 - H_{298}^0)$ is enthalpy at T temperature, defined relatively enthalpy at temperature 298K, T is temperature in °C degrees, C_p is heat capacity, $(G_T^0 - H_{298}^0)$ is Gibbs energy, $\Delta_f G_T^0$ is Gibbs energy for element f at T temperature, $\Delta_f H_T^0$ is enthalpy for f element at T temperature.

The standard error of experimental data is defined by the formula:

$$\delta = \frac{2[\sum(x_i - x_m)^2]}{\sqrt{n(n-1)}}$$

where is value from the experimental data, x_m is average value of all experimental data, n is quantity of measurements.

The thermodynamic data on $Ni_xZn_{1-x}Fe_2O_4$ ferrites and their temperature dependences obtained in the present paper are given in Tables 1-4.

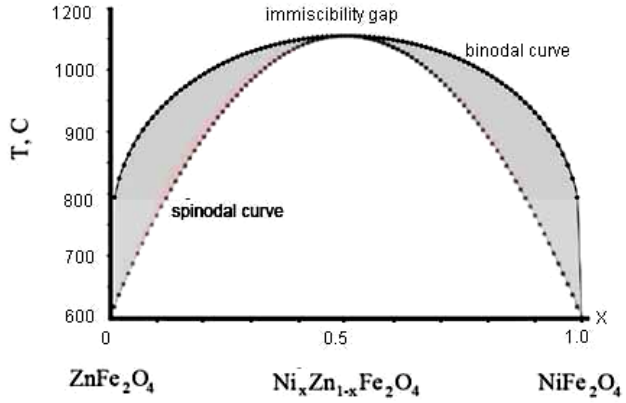

Fig. 1. The state diagram $Ni_xZn_{1-x}Fe_2O_4$ in temperature interval 950°C-1180°C.

Table 1. The data on initial substances for theoretical calculations of thermodynamical parameters.

	Fe_2O_3	NiO	Zn0	$ZnFe_2O_4$	$NiFe_2O_4$
Melting point, K	1895	2257	2242	1278	1938
Molar volume, cm^3	30.27	10.97	14.34	44.94	43.65
$H_{298}^0 - H_0^0, kJ$	65.10	6.69	6.93	-	-
A	$-8.089*10^2$	$-2.331*10^2$	-	$-1.167*10^3$	$-1.053*10^3$
B	$2.466*10^{-1}$	$8.392*10^{-2}$	-	$3.112*10^{-1}$	$3.232*10^{-1}$
C	$-8.423*10^5$	$-2.850*10^5$	-	$-7.364*10^5$	$-8.04*10^5$
A1	$1.50147*10^3$	-8.776	4.350*10		
A2 (T)	-1.2146*10	$4.223*10^{-2}$	$7.658*10^{-3}$		
A3 (T^{-2})	$1.4123*10^7$	$3.607*10^6$	$-7.573*10^5$		
A4 ($T^{-0.5}$)	$-2.1493*10^4$	$7.873*10^{-2}$	5.456*10		
A5(T^2)	$5.690*10^{-4}$	$-7.526*10^{-6}$	-		

Table 2. The heats of formation and entropy at temperature 298K and normal pressure for $Ni_xZn_{1-x}Fe_2O_4$ ferrite components

	ΔH_{298}^0, кJ/mol	S_{298}^0, J/(mol·deg)	ΔG_{f298}^0, kJ/mol
Fe_2O_3	-826.2	88.04	-743.9
NiO	-239.3	38.27	-211,0
Zn0	-350.5	43.45	-320.2
$ZnFe_2O_4$	-1188.0	151.90	-1081.5
$NiFe_2O_4$	-1070.5	141.81	-964.5

Table 3. Temperature dependences of thermodynamic parameters of initial components of $Ni_xZn_{1-x}Fe_2O_4$ solid solutions

$C_p^0, \frac{J}{mol \cdot deg}$				$S_T^0, \frac{J}{mol \cdot deg}$		
T,K	Fe_2O_3	NiO	ZnO	Fe_2O_3	NiO	ZnO
300	104.32	44.70	40.53	88.04	38.27	43.45
400	120.29	53.00	44.56	120.27	52.38	55.73
500	131.72	64.90	46.74	148.44	65.25	65.93
600	139.33	56.01	48.22	173.16	76.07	74.59
700	146.52	54.22	49.38	195.17	84.55	82.11
800	156.12	53.66	50.37	215.32	91.74	88.77
900	170.22	53.83	51.28	234.47	98.06	94.76
1000	148.49	54.43	52.13	266.18	103.76	100.20
1100	143.55	55.29	52.94	278.53	108.99	105.21
1200	140.74	56.29	53.74	278.53	113.84	109.85
1300	140.07	57.37	54.52	289.76	118.39	114.18
1400	141.42	58.48	55.29	300.18	122.68	118.25
$\frac{(H_T^0 - H_{298}^0)}{T}, \frac{J}{mol \cdot deg}$				$-\frac{(G_T^0 - H_{298}^0)}{T}, \frac{J}{mol \cdot deg}$		
300	0.64	0.28	0.25	87.40	37.99	43.20
400	28.59	12.52	10.89	91.68	39.86	44.85
500	48.16	21.59	17.86	100.28	43.66	48.07
600	62.75	27.86	22.80	110.41	48.21	51.79
700	74.19	31.73	26.52	120.98	52.82	55.60
800	83.79	34.50	29.44	131.53	57.24	59.34
900	92.57	36.63	31.81	141.90	61.43	62.94
1000	100.16	38.38	33.80	152.11	65.38	66.40
1100	104.32	39.88	35.51	161.86	69.11	69.71
1200	107.45	41.20	36.99	171.08	72.64	72.86
1300	109.18	42.40	38.31	179.78	75.99	75.87
1400	112.16	43.51	39.50	188.02	79.17	78.76
$\Delta_f H^0, \frac{\text{kJ}}{mol}$				$\Delta_f G^0, \frac{\text{kJ}}{mol}$		
300	-826.2	-239.3	-350.5	-743.9	-211.0	-320.2
400	-824.6	-238.6	-350.3	-716.6	-201.6	-310.1
500	-822.3	-237.3	-349.9	-689.9	-192.5	-300.1
600	-819.6	-236.2	-349.6	-663.6	-183.6	-290.2
700	-816.9	-235.6	-356.6	-637.8	-175.0	-280.2
800	-814.0	-235.1	-356.4	-612.4	-166.8	-269.4
900	-810.9	-234.5	-356.1	-587.4	-157.8	-258.5
1000	-808.9	-234.0	-355.8	-562.8	-149.3	-247.7
1100	-810.8	-233.5	-355.5	-538.0	-140.8	-236.9
1200	-811.9	-233.1	-470.2	-513.2	-132.4	-224.2
1300	-910.1	-232.6	-468.6	-488.4	-124.0	-203.7
1400	-808.5	-232.1	-467.0	-463.8	-115.7	-183.4
$Log\ K_f$						
300	129.51	36.73	55.75			
400	93.58	26.33	40.49			
500	72.07	20.11	31.35			
600	57.77	15.99	25.26			
700	47.59	13.05	20.91			
800	39.99	10.89	17.59			
900	34.09	9.16	15.00			
1000	29.40	7.80	12.94			
1100	25.55	6.69	11.25			
1200	22.34	5.76	9.75			
1300	19.62	4.98	8.18			
1400	17.30	4.32	6.84			

Table 4. Temperature dependences of thermodynamic parameters of $Ni_xZn_{1-x}Fe_2O_4$ solid solutions

$C_p^0, \frac{J}{mol \cdot deg}$					
T,K	$ZnFe_2O_4$	$Ni_{0.25}Zn_{0.75}Fe_2O_4$	$Ni_{0.5}Zn_{0.5}Fe_2O_4$	$Ni_{0.75}Zn_{0.25}Fe_2O_4$	$NiFe_2O_4$
300	193.61	182.002	170.395	158.788	147.18
400	203.23	193.433	183.635	173.837	164.04
500	209.32	202.24	195.16	188.08	181.00
600	214.01	210.007	206.005	202.002	198.00
700	219.0	218.005	217.01	216.015	215.02
800	223.11	225.262	227.525	229.788	232.05
900	226.5	232.148	237.795	243.442	249.09
1000	229.0	238.282	247.565	256.847	266.13
1100	-	244.5	257.01	269.5	282.05
$S_T^0, \frac{J}{mol \cdot deg}$					
300	151.90	149.377	146.855	144.333	141.81
400	209.05	203.403	197.755	192.108	186.46
500	255.09	247.538	239.985	232.433	224.88
600	293.68	285.105	276.530	267.955	259.38
700	330.02	320.31	310.600	300.890	291.18
800	363.97	353.23	342.490	331.750	321.01
900	394.03	382.83	371.660	360.490	349.32
1000	420.11	409.195	398.280	387.365	376.45
1100	-	428.653	418.435	408.217	398.00
$\frac{(H_T^0 - H_{298}^0)}{T}, \frac{J}{mol \cdot deg}$					
300	1.19	1.12	1.05	0.98	0.91
400	50.62	47.86	45.10	42.34	39.58
500	81.78	77.88	73.97	70.07	66.17
600	103.44	99.26	95.08	90.90	86.72
700	121.06	116.75	112.45	108.14	103.83
800	137.12	132.54	127.96	123.38	118.80
900	151.96	147.05	142.14	137.24	132.33
1000	162.02	157.73	153.44	149.15	144.86
1100	-	160.25	156.50	152.75	149.00
$-\frac{(G_T^0 - H_{298}^0)}{T}, \frac{J}{mol \cdot deg}$					
300	150.70	148.25	145.80	143.35	140.90
400	158.43	155.54	152.65	149.77	146.88
500	173.31	169.66	166.01	162.36	158.71
600	190.24	185.82	181.40	176.98	172.56
700	208.00	202.84	197.67	192.51	187.35
800	227.03	220.80	214.61	208.41	202.21
900	246.91	239.50	232.00	224.50	217.00
1000	268.31	258.90	249.79	240.69	231.59
1100	-	279.25	268.50	257.75	247.00
$\Delta_f H^0 \cdot 10^3, \frac{\text{kJ}}{mol}$					
T,K	$ZnFe_2O_4$	$Ni_{0.25}Zn_{0.75}Fe_2O_4$	$Ni_{0.5}Zn_{0.5}Fe_2O_4$	$Ni_{0.75}Zn_{0.25}Fe_2O_4$	$NiFe_2O_4$
300	-1.188	-1.159	-1.129	-1.100	-1.071
400	-1.182	-1.154	-1.125	-1.097	-1.069
500	-1.176	-1.148	-1.121	-1.094	-1.066
600	-1.170	-1.143	-1.117	-1.090	-1.063
700	-1.163	-1.137	-1.111	-1.085	-1.059
800	-1.157	-1.131	-1.105	-1.081	-1.054
900	-1.151	-1.125	-1.099	-1.073	-1.048
1000	-1.145	-1.119	-1.093	-1.067	-1.042
1100	-	-1.113	-1.087	-1.061	-1.035

$\Delta_f G^0, \frac{\text{kJ}}{mol}$					
300	-1081.5	-1052.0	-1023.2	-993.75	-964.5
400	-1046.9	-1018.1	-988.15	-958.78	-929.4
500	-1013.9	-984.12	-954.35	-924.58	-894.8
600	-982.0	-951.68	-921.35	-891.03	-860.7
700	-950.2	-919.33	-888.65	-857.97	-827.3
800	-919.5	-888.00	-857.07	-826.3	-795.0
900	-888.3	-856.63	-825.25	-793.88	-762.5
1000	-850.7	-820.28	-790.55	-760.83	-731.1
1100	-	-789.25	-759.51	-729.75	-700.0
$Log\ K_f$					
300	188.30	183.21	178.12	173.02	167.93
400	136.71	132.87	129.04	125.20	121.36
500	105.91	102.80	99.69	96.58	93.47
600	85.49	82.85	80.21	77.57	74.93
700	73.03	70.18	67.37	64.55	61.73
800	61.00	58.73	56.46	54.18	51.91
900	51.01	49.31	47.63	45.94	44.25
1000	43.20	41.80	40.59	39.39	38.19
1100	-	36.01	34.97	34.03	33.00

[1] *N.R. Babayeva*, "The suppression of high-frequency overvoltages in high-voltage electrical circuits and devices," Problems of power engineering, №4, 2005, pp.4-47, (in Russian).

[2] *A.M. Gashimov, T.R.Mehdiyev, N.R. Babayeva,* "Frequency-dependent resistor," International conference «Physics-2005», Baku, June 7-9, 2005, pp.613-617, (in Russian).

[3] *A.M. Gashimov, T.R. Mehdiyev, N.R. Babayeva,* "The possibilities of high-frequency overvoltage limitation by the using of the frequency- dependent resistor," International conference energy of Moldova-2005, Kishinev, 21-24 September 2005, pp.265-269, (in Russian).

[4] *A.M. Gashimov, T.R. Mehdiyev, N.R. Babayeva*, "Effect of magnetic multi-layer to resistive properties of frequency-dependent resistor," TPE-2006, 3rd International conference on Technical and Physical Problems in Power Engineering, Ankara, Turkey 29-31 may 2006, p. 604-606.

[5] *N.R. Babayeva*, "The algorithm of high-frequency overvoltages at use in patching circuit of frequency-dependent resistor," Problems of power engineering, №3-4, 2006, pp.32-37, (in Russian).

[6] *A.M. Hashimov, T.R. Mehdiyev, N.R. Babayeva*, "The electric and heat characteristics of frequency-dependent resistor," Fizika, №4,vol.XII,2006,p.28-32.

[7] *A.M. Gashimov, T.R.Mehdiyev, N.R. Babayeva*, "On appropriateness of use of frequency-dependent resistor at limitation of high-frequency Overvoltages," Modern Electric Power Systems"06, Wroclaw, Poland, Sept. 6-8, 2006, p.379-382.

[8] *E.V.Dmitriyev, A.M.Gashimov, T.R.Mehdiyev, N.R. Babayeva,* "The heat parameters and functioning regime of frequency-dependent resistor," Scientific conference dedicated to memory of U.N.Vershinin "Electro-physics of materials and installations", Novosibirsk, January, 9-12, 2007, pp.55-60, (in Russian).

[9] *N.R.Babayeva, A.M.Gashimov, E.V.Dmitriyev, T.R.Mehdiyev*, "The study of skin-effect and heat regimes of frequency-dependent resistor work," Fizika, № 1-2, vol. XIII, 2007, p.102-107, (in Russian).

[10] *N.R.Babayeva, A.M.Gashimov, T.R.Mehdiyev*, "About some peculiarities of current passage through frequency-dependent resistor," Fizika, №4, vol. XIII, 2007, p.230-235, (in Russian).

[11] *V.G.Kuznecov, T.R.Mehdiyev, N.R. Babayeva,* "To calculation of frequency-dependent resistor characteristics," Technical electrodynamics, Kiyiv, 2007, pp.88-91, (in Russian).

[12] *T.R.Mehdiyev, N.R. Babayeva, A.M.Gashimov, A.A. Habibzade,* "Electromagnetic processes in frequency-dependent resistor shell," Fizika, №2, vol. XIV, 2008, pp.80-87, (in Russian).

[13] *T.R. Mehdiyev, A.M.Gashimov, N.R.Babayeva, A.A.Habibzade,* "Electric and magnetic properties of frequency-dependent resistor shell," Fizika, №3, vol. XIV, 2008, pp.207-217, (in Russian).

[14] *T.R.Mehdiyev, A.M. Gashimov, N.R. Babayeva, Y.V.Dmitriyev, A.A.Habibzadeh,* "The peculiarities of current passing through frequency dependent resistor," 4-th International Conference on Technical and Physical Problems of Power Engineering TPE-2008, 4-6 September 2008, Pitesti, Romania, II-4 – II-8

[15] *A.A.Habibzadeh, T.R.Mehdiyev, A.M. Hashimov, E.V. Dmitriyev, N.R.Babayeva,* "Dependence of electrical and magnetic properties of frequency-dependent resistor shell on ferromagnetic granule concentration and dimension," 5-th International Conference on Technical and Physical Problems of Power Engineering TPE-2009, 3-5 September 2009, Bilbao, Spain, p.228-232

[16] *H. Habibzadeh, T.R. Mehdiyev, A.M. Hashimov, E.V. Dmitriyev and N. R. Babayeva*, "Influence of concentration and the sizes of ferromagnetic granules on electrical and magnetic properties of FD-resistor shell," International Journal for Knowledge, Science and Technology, v.1, N 1, 2009, p.49-56

[17] *Arif M. Gashimov, Narmin R. Babayeva, Talat R. Mehdiyev*. Magnetoelectric and Magnetoelastic of Frequency-Dependent Resistor Properties of Ferromagnetic Shell, Modern Electric Power Systems"06, Wroclaw, Poland, Sept. 20-22, 2010, p.56

[18] *H. Habibzadeh, N.R. Babayeva, A.M. Hashimov, T.R. Mehdiyev.* Magnetoelectric and magnetoelasic properties of ferromagnetic shell of frequency dependent resistor, 6-th International Conference on Technical and Physical Problems of Power Engineering TPE-2010, 14-16 September 2010, Tabriz, Iran, p.617-621

[19] *Sh.N. Aliyeva.* The magnetic properties of $Zn_xNi_{1-x}Fe_2O_4$ solid solution, Fizika, № 1, vol. XVII, 2011, pp.6-9.

[20] *Sh.N. Aliyeva, A.S. Amirov, N.R. Babayeva, T.R. Mehdiyev* The composite magnetic properties with $Ni_xZn_{1-x}Fe_2O_4$ filler, 7th International Conference ICTPE, 7-9 July 2011, Lefkosa, TR Northern Cyprus, p.327-332

[21] Kratkiy spravochnik phizico-khimicheskikh velichin. *Pod. red. A.A. Ravdelya i A.M. Ponomaryovoy*. Izdanie desyatoe, Sankt-Peterburg, 1999, 231s.

[22] Ray Siba P., Liu Xinghua, Weirauch Douglas A. Cermet inert anode containing oxide and metal phases useful for the electrolytic production of metals. European Patent Application, EP 1 666 640 A2, 2006, Bulletin 2006/23, 30c.

Received:24.10.2011

NANOSECOND DISCHARGES IN A NONUNIFORM ELECTRIC FIELD

ARIF HASHIMOV, RAUF MEKHTIZADEH,
ALEKSEY BONDYAKOV, SHAMIL KAZIMOV
G.M. Abdullayev Institute of Physics of Azerbaijan National Academy of Sciences,
Az-1143, Baku, Javid str. 33
e-mail: zxalex_physics@yahoo.com

High pressure nanosecond diffuse discharges in a nonuniform electric field are studied experimentally using a recording system. The local and non-local criterions of runoff electrons in gases and formation the powerful electron beams on the discharge gap are considered. Conversion of diffusive volume discharge to contracted discharge at different interelectrode distance and electrodes geometry is considered.

Keywods: Nanosecond discharge, nonuniform electric field
PACS: 51.50.+v - 52.80.Mg

Introduction

Pulsed elevated pressure diffuse discharges are today widely used in science and technology, for example, in the production of gas and plasma lasers [1–3] and avalanche switches [4]. To initiate a diffuse discharge, variously designed preionization sources and discharge gaps with a uniform electric field are usually used. However, it has been known since the late 1960s that, under atmospheric pressure, a diffuse discharge in different gases can be initiated without a preionization source [5, 6]. To this end, short high voltage pulses and a discharge gap the cathode of which has a small radius of curvature should be applied. Atmospheric pressure diffuse discharges were initiated in helium [5] and air [6]. These discharges are known to generate X rays [5, 6] and runaway electron beams [7]. Nevertheless, they remain poorly studied, because it is difficult to measure their parameters and also the parameters of attendant runaway electron beams and subnanosecond X ray pulses [8].
Switchover of a streamer channel to a spark one continues to attract the attention of researchers [9] because of the complexity of this phenomenon and short transients. It was suggested [9] that a streamer closing the discharge gap generates an electric field that is high enough to result in field emission, which gives rise to processes that turn the streamer channel into a spark one. It was shown in monograph [10] that the contraction of a volume discharge in a wide range of experimental conditions is related to the emergence of cathode spots caused by explosive electron emission. At high pressures of gas mixtures, a volume discharge was initiated owing to preionization from additional sources. Then, channels propagating from the cathode spots toward the anode bridged the gap.

Recently, high pressure nanosecond discharges initiated in a nonuniform electric field have become a subject of extensive research [3–9]. Under such conditions, diffuse discharges are initiated without additional sources preionizing the gap. A feature of discharges in a nonuniform electric field is the generation of X rays and runaway electron beams, which were detected behind the anodes of gas filled diodes [7, 8]. It was suggested [9] that diffuse discharges initiated without additional preionization sources can be called runaway electron preionized diffuse discharges (REP discharges). In the point–plane geometry of the gap, cathode spots in the REP discharge arise within less than 1 ns [8]. It could be expect that the fast appearance of cathode spots will result in the formation of a spark channel. However, diffuse discharge to spark discharge switchover in a nonuniform electric field at high values of reduced electric field E/p and under the conditions of runaway electron generation have not been studied to date.

Experimental results

Appearance of runaway electrons in gases takes on special significance in view of getting the powerful subnanosecond electron beams with record big current amplitude [8]. Space structure of discharge gap's glow during the pulsed discharge process is defined by some factors such as the electrodes geometry, pressure and type of gas, inductive and capacitive parameters of generator, and breakdown voltage of discharger – peaker [9].
In spite of rapid growth of experimental researches and technical applications [10] of nanosecond discharges in gases, transition to the new time scale doesn't entail the corresponding revision of fundamental positions of breakdown classical models developed for conditions near the static ones [11]. But in article [10] the new understandings of nanosecond pulsed discharges are determined.

Electrical breakdown models in dense gases differed from each other in many respects, sometime radically, nevertheless have common fundamental feature: they are local. It means that on given point of space - time (r, t) the average statistical value such as an electrons energy-ε_e, ordered motion speed - ν and Townsend ionization factor - α are determined by local field at the same point $E(r,t) = E_o + E_p(r,t)$, where E_o and $E_p = E_{p+} + E_{p-}$ are external field and field of space charges.
To local models are related the model of Townsend avalanche generation with γ-processes on cathode and different modifications of single-avalanche streamer model that describes the breakdown processes in dense gases corresponding to right arm of Pashen's curve ($pd >> (pd)_{min}$), in the cases when the space charge Z_{cr} and time t_{cr} scales of avalanche progress up to critical values satisfy to correlations:

$$t_{cr} \le \frac{d}{\upsilon_-} \qquad (2)$$

where N_E^{cr} is electrons quantity in the critical avalanche, d is interelectrode distance.

In classical streamer model it can be sort out three main parts: increase of electrical field on the electron avalanches fronts and streamers as result of their polarization ($E_f=E_o + E_p$); gas ionization by photons ahead of fronts; prevalent of ionization processes in the gas volume in comparison with cathode emission.

As result of field increasing the electrons energy becomes much more than ε (E_o), owing to which the ionization processes are intensified.

Volumetric photoionization explains the big speed of streamers propagation ($>> \nu_- (E_o)$) and it is necessary for propagation of cathode streamer. The question of the nature of radiation initiating the second ionization centers out of initial avalanche [12,13] is opened to discussion. In this article all these questions are considered.

In case of large interelectrode distance even for very strong fields, where field intensity exceeds a critical value, the Townsend's ionization mechanism is also true that includes the γ - processes on cathode and streamers formation, by means of which the ionization processes in gases corresponding to right arm of the Pashen's curve ($pd >> (pd)_{min}$) are described.

In this case for determination of average energy E^*, it is necessary to take into account a number of electrons by $E > E_{cr}$, as is shown below:

$$\frac{d\left(N_e E^*\right)}{dx} = eEN_e - F\left(E^*\right)N_e \qquad (3)$$

$$\frac{dN_e}{dx} = \alpha_i \cdot N_e \qquad (4)$$

$$\frac{dE^*}{dx} = eE - F(E^*) - \alpha_i E^* \qquad (5)$$

where α_i is a collision ionization factor, E^* is electrons average energy.

In formula (5) we can see that even by full neglect of electrons deceleration in gas $F(E^*) = 0$, the average energy of electrons is restricted

$$E^* < E^*_{\max} = \frac{eE}{\alpha} \qquad (6)$$

At sufficiently big overvoltages ($\Delta >> 1$) development of gas discharge process is differed from classical discharge forms in gases.

In strongly overstrained discharge gaps an avalanche-streamer transition is realized on the length of $z_{cr} \sim 100\,\mu$. As a result of that a plasma cloud by big conductivity is formed. Being in strong electrical fields this cloud is polarized. Then ionization is developed for account of electrons escaping from cloud and accelerating in space charge zone. Part of these electrons has very big energy comparable with full kinetic energy $eU = eEd$ and uninterruptedly accelerated up to anode. These electrons efficiently radiate the braking quantum ionizing gas in the whole discharge gap and knocking out the electrons from electrodes. As a result of that a number of the elementary "accelerators" increases.

The experiments in uniform and non-uniform electrical fields at big pressures and different gases (nitrogen, air, helium, neon, argon, and krypton) without the ionization source were carried out [14].

In all gases in non-uniform electrical field at the atmospheric conditions under the influence of high voltage nanosecond pulses the high specific energy up to $1 J/cm^3$ and electron beams by record current amplitude were received.

The run off electrons ensure the high propagation speed of ionized field to anode and attendant X-radiation ionizes gas and causes a photoelectric effect on cathode stipulated for motion the cathode streamer.

Our researches were carried out by means of high voltage nanosecond generator by 60 kV with short pulse front about 25 ns. (Fig.1). Measurements were carried out only after bombardment of a surface of electrodes by several hundreds high voltage impulses.

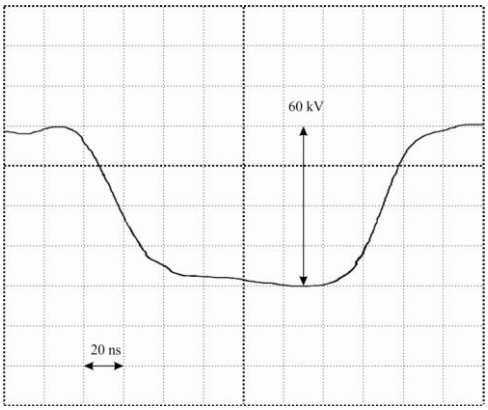

Fig.1. Oscillogram of high-voltage pulse

On Fig.2. a block scheme of an experimental installation is shown. Impulse voltage was supplied from generator 1 to high voltage electrode – cathode 3 inside the vacuum chamber 2 at atmospheric pressure at air – P=760 Torr. Two cathodes by different curvature radius – $r_c \sim 1$ and 6 mm were used. For obtaining the glow of volumetric pulsed discharge at atmospheric and higher pressure a Teflon cap 6 was installed on cathode by diameter ∅ 1 mm. As an anode the copperplate 4 and metal netting 5 were used. Interelectrode distance ~d was changed over the range ~ 3-10 mm. For photographing of the high speed pulsed discharge glow an electron-optical camera 7 was used.

The total current of pulsed discharge was registered by high-frequency oscillograph TDS-5104 by means of current shunt 8. Electron beam's current was also registered by means of Faraday cup and current shunt 9.

The cathode and cathode plasma are the sources of runaway electrons in air at atmosphere pressure. Dispersion on gas molecules strongly influences on the space distribution of runaway electrons. In case of pointed cathode the interelectrode distance – d greatly influences

on the width of runaway electrons beam. At increase the - *d* up to 10 mm beam's diameter reaches to ∅ ~3cm.

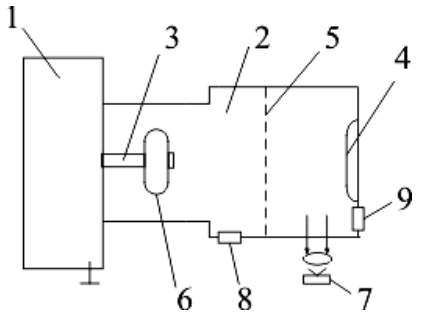

Fig.2. Block scheme of an experimental assembly
1- high voltage nanosecond generator, 2 –vacuum chamber, 3 –cathode, 4 – anode, 5 – metal netting, 6 – fluoroplastic cap, 7 – electron-optical camera, 8 – shunt for measuring of discharge total current, 9 – shunt for measuring of electron beam's current.

If there are some channels in pulsed discharge, that taking place for cathodes with developed surface, the channels quantity are equal to beams quantity in electron stream behind the anode. The streams structure respond to distribution of cathode emitting centers.

Plasma bunch on cathode is transformed into constricted channel growing deep into discharge gap by the stream of runaway electrons. Variety of discharges space forms is explained by statistic of this interaction and by statistic of electron avalanches initiation. When overvoltage factor $\Delta >> 1$, the gas breakdown is initiated by auto electronic emission and the first avalanche reaches a critical size near the initialization point ($Z_{cr} \sim 100\,\mu$ << d). As a result the strengthening of positive space charge field E_{p+} and auto electronic emission are taking place. Therefore, when $\Delta >> 1$, the emissive processes play a fundamental role in propagation of ionization towards the cathode. The high penetrability of runaway electrons and X-ray radiation lead to ionization of dense gas far off the first ionization centers and discharge loses its compact form acquiring the diffusive or multi-channel character.

At high overvoltages in dense gases at atmosphere pressure the complex space structure of the nanosecond volumetric discharges as the constricted channels is explained by electrons acceleration in space charge field. These electrons are permitted to accelerate up to anode. They radiate the quantum ionizing the gas in whole discharge gap and battering the electrons from electrodes.

The space structure of discharge gap's glow, as mentioned above, is determined by some parameters such as electrodes geometry, interelectrode distance – *d*, gas pressure – p and parameters of generator.

The photography of discharge gap's glow for different distance values – d and electrodes geometry are presented on figures 3. On figures a flat copperplate and metal netting are as an anode and a metal rod with different radiuses of curvature – $r_к$ ~1-6 mm is as a cathode. It is shown on Fig. 3, that in atmosphere pressure, at U_{gen} = 60 kV and *d*=10 mm the diffusive volumetric discharge is realized.

Fig. 3. r_k= 6 mm, anode - copperplate, U_{gen}=60 kV, P=760 Torr, interelectrode distance d=10 mm

It is known that the discharge plasma is a source of X rays, runaway electron beams, and optical radiation in different spectral ranges [8-17]. In this work, we also detected X rays and an ultrashort avalanche electron beam behind the foil and the discharge plasma was a source of powerful spontaneous radiation. For the generator, the maximal amplitude of the beam current behind the 20 μm thick copper netting was about 27 A for a 9 mm wide gap. The exposure dose of the X ray radiation behind the foil was 0.6 mR.

The X ray pulse from the discharge chamber was found to be about 0.2 ns, which is the ultimate time resolution of the diamond detector. These parameters of the electron beam and X ray radiation were obtained for voltage pulse duration of 200 ns. As the voltage pulse shrank to 100 ns or less, the amplitude of the runaway electron beam current, the exposure dose of the X ray radiation, and the energy of runaway electrons decreased.

Conclusions

We studied the breakdown of gaps with a nonuniform electric field distribution in atmosphere of air. Breakdown was initiated by applying high voltage pulses with duration of 25 ns from 200 ns. The shrinkage of the voltage pulse extends the conditions for diffuse (volume) discharge initiation without preionization. The volume discharge is initiated owing to the preionization of the gap by runaway electrons and X ray photons. When the electrode with a small radius of curvature is under a negative potential, the formation of a diffuse (volume) discharge is due to preionization by runaway electrons, which are generated in the discharge gap because the field enhancement near the cathode and in the gap. When this electrode is under a positive potential, the X ray radiation due to runaway electron slowdown at the anode and in the gap plays a major role in the formation of the volume discharge.

[1] *Gas Lasers, Ed. by E. W. McDaniel and W. L. Nighan* (Academic, New York, 1982).
[2] *G. A. Mesyats, V. V. Osipov, and V. F. Tarasenko,* Pulsed Gas Lasers (Nauka, Moscow, 1991; SPIE, Washington,1995).
[3] *Gas Lasers*, *Ed. by I. Endo and R. F. Walter* (CRC, Boca Raton, 2007).
[4] *G. A. Mesyats,* Pulsed Power (Nauka, Moscow, 2004;Springer, Berlin, 2004).
[5] *R. C. Noggle, E. P. Krider, and J. R. Wayland,* J. Appl.Phys. 39, 4746 (1968).
[6] *L. V. Tarasova, and L. N. Khudyakova,* Zh. Tekh. Fiz.39, 1530 (1969) [Sov. Phys. Tech. Phys. 14, 1148 (1969)].
[7] *L. V. Tarasova, L. N. Khudyakova, T. V. Loiko, and V. A. Tsukerman,* Zh. Tekh. Fiz. 44, 564 (1974) [Sov. Phys. Tech. Phys. 19, 351 (1974)].
[8] *V. F. Tarasenko, E. K. Baksht, A. G.Burachenko,I. D. Kostyrya, M. I. Lomaev, and D. V. Rybka,* Plasma Devices Op. 16, 267 (2008).
[9] *I. D. Kostyrya, V. S. Skakun, V. F. Tarasenko, and A. V. Fedenev,* Zh. Tekh. Fiz. 74 (8), 35 (2004) [Tech. Phys. 49, 987 (2004)].
[10] *S. B. Alekseev, V. P. Gubanov, I. D. Kostyrya, V. M. Orlovskii, V. S. Skakun, and V. F. Tarasenko,* Kvantovaya Elektron. (Moscow) 34, 1007 (2004) [Quantum Electronics 34, 1007 (2004)].
[11] *I. D. Kostyrya and V. F. Tarasenko,* Izv. Vyssh. Uchebn. Zaved., Fiz., No. 12, 85 (2004) [Russian Physics Jour nal 47, 1314 (2004)].
[12] *I. D. Kostyrya, V. M. Orlovskii, V. F. Tarasenko, F. N. Tkachev, and S. I. Yakovlenko,* Zh. Tekh. Fiz. 75 (7), 65 (2005) [Tech. Phys. 50, 881 (2005)].
[13] *E. Kh. Baksht, V. F. Tarasenko, M. I. Lomaev, and D. V. Rybka,* Pis'ma Zh. Tekh. Fiz. 33 (9), 29 (2007) [Tech. Phys. Lett. 33, 373 (2007)].
[14] *V. V. Bratchikov, K. A. Gagarinov, I. D. Kostyrya, V. F. Tarasenko, A. N. Tkachev, and S. I. Yakovlenko,* Zh. Tekh. Fiz. 77 (7), 34 (2007) [Tech. Phys. 52, 856 (2007)].
[15] *R.N. Mehdizadeh , A.S. Bondyakov , Sh.A. Kazumov*. Numerical simulation of cathode streamer in pulse discharge. "Power engineering problems" 2009 №1, p.49-54
[16] *A.M.Gashimov, R.N. Mekhtizadeh, E.J.Gurbanov, A.S. Bondyakov*: Int. Conference "Physics-2005", Baku (2005) 450
[17] *Yu.N. Vershinin, A.M.Gashimov, E.J.Gurbanov:* SEAE (2005) No.6, 72

Received:10.10.2011

EXPERIMENTAL AND THEORETICAL ^{15}N NMR AND $^{1}J_{CH}$ SPIN-SPIN COUPLING CONSTANTS INVESTIGATION OF 4-(3-CYCLOHEXEN-1-YL)PYRIDINE

ÖZGÜR ALVER [1], MEHMET FATİH KAYA [2] AND CEMAL PARLAK [2]

[1] Department of Physics, Science Faculty, Anadolu University, Eskişehir, 26470, Turkey

[2] Department of Physics, Dumlupınar University, Kütahya, 43100, Turkey

E-mail: cparlak20@gmail.com, Tel.: +90 (274) 265 20 51 / 3116, Fax: +90 (274) 265 20 56

The magnitude of one bond $^{1}J_{CH}$ coupling constants and ^{15}N NMR spectrum of 4-(3-Cyclohexen-1-yl)pyridine (4-Chpy) have been reported for the first time. ^{15}N NMR chemical shift and $^{1}J_{CH}$ coupling constants of 4-Chpy ($C_{11}H_{13}N$) have been calculated by means of the Becke-3-Lee-Yang-Parr (B3LYP) density functional method with 6-311++G(d,p) basis set. Comparison between experimental and theoretical results indicates that density functional B3LYP method is in good agreement with the experimental NMR data.

Keywords: 4-(3-Cyclohexen-1-yl)pyridine, Coupling Constant, NMR, DFT.
PACS: 31.15. E, 33.25.+k

1. INTRODUCTION

4-(3-Cyclohexen-1-ly)pyridine molecule is mainly composed of pyridine which is a basic heterocyclic organic compound with the chemical formula C_5H_5N and cyclohexene which is a hydrocarbon with the formula C_6H_{10}. Previously, we reported some experimental and theoretical infrared and NMR spectroscopic properties of 4-Chpy [1, 2]. We also prepared Hofmann-type complexes by using this molecule as a ligand in our previous study [2].

DFT methods with GIAO (Gauge Including Atomic Orbitals) approach is widely used for the calculations of chemical shifts for different types of compounds [1, 3-6]. During the last decade an important breakthrough in the calculation of NMR spin-spin coupling constants took place when the coupled-perturbed approach was implemented within the DFT framework [5, 6]. At present with this methodology an interesting variety of spin-spin coupling constants can be calculated with good accuracy in polyatomic systems using reasonable computational resources [7].

As continuation our NMR studies on 4-Chpy, we wish to extend investigations using the different NMR techniques. In this work, in order to get a deeper insight into the electronic structure of 4-Chpy and to see the hybridization and type of the bond effects on $^{1}J_{CH}$ coupling constants, we have decided to measure $^{1}J_{CH}$ values. Hence, we have reported the magnitude of one bond $^{1}J_{CH}$ coupling constants, proton coupled ^{13}C NMR and ^{15}N NMR spectra of the title molecule for the first time. ^{15}N NMR chemical shift and the magnitude of one bond $^{1}J_{CH}$ coupling constants of 4-Chpy have been calculated by using B3LYP method with 6-311++G(d,p) basis set.

2. EXPERIMENTAL

The pure 4-Chpy in the liquid form was obtained from Aldrich Chemical Co. and used without further purification. NMR experiments were performed in Bruker AVANCE 500 spectrometer using 5 mm BBO probe at 300 K. In order to prevent the overlapping of the solvent and sample peaks, 4-Chpy was dissolved in MeOD. Chemical shifts were reported in ppm relative to TMS and formamide for proton coupled ^{13}C NMR and ^{15}N NMR spectra, respectively. Proton coupled ^{13}C NMR and ^{15}N NMR spectra were obtained at a base frequency of 125.76 MHz for ^{13}C and 50.66 MHz for ^{15}N nuclei. For proton coupled ^{13}C NMR spectroscopy, the pulse sequence used a delay (D1) and acquisition time (AQ) of 2.0 s and 1.1 s, respectively, a spectral width of 29761.90 Hz, 64K data points, 900 pulse (8.30 µs) and 16 scans. For ^{15}N NMR spectroscopy, the pulse sequence used a delay (D1) and acquisition time (AQ) of 5.0 s and 0.64 s, respectively, a spectral width of 25510.20 Hz, 32K data points, 900 pulse (15.00 µs) and 2000 scans.

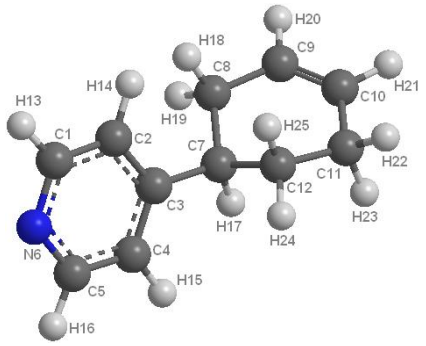

Fig. 1. Optimized molecular structure of 4-Chpy.

Table 1. ^{15}N NMR shifts (ppm) and $^{1}J_{CH}$ coupling constants (Hz) of 4-Chpy.

$^{1}J(C_nH_n)$ / Hybridization	Experimental	B3LYP
C_1H_{13}, C_5H_{16} / sp^2	175.25	171.15
C_9H_{20} / sp^2	163.12	158.88
C_2H_{14}, C_4H_{15} / sp^2	161.08	155.65
$C_{10}H_{21}$ / sp^2	156.02	151.36
$C_8H_{18}H_{19}$ / sp^3	129.14	125.91
C_{12} $H_{24}H_{25}$ / sp^3	126.06	124.55
C_7 H_{17} / sp^3	125.01	123.38
$C_{11}H_{22}H_{23}$ / sp^3	124.32	122.83
^{15}N NMR		
N_6	192.14	202.35

$^{1}J_{CH}$ coupling constants for the title molecule are derived from the proton coupled ^{13}C NMR spectrum of this molecule (Figure 2). Due to electronegative effect of the nitrogen atom, it is clearly seen in 4-Chpy molecule that C_1-H_{13} and C_5-H_{16} have stronger coupling constants when compared the other C-H couplings in this molecule. Furthermore, C_9 and C_{10} carbon atoms show sp^2 hybridization so they have stronger C-H coupling constants in the cyclohexen ring since the other carbons in this ring have sp^3 type hybridization.

3. CALCULATION

For the NMR calculations, molecular structure of 4-Chpy was first fully optimized at 6-31G(d) level in methanol (ε = 32.63) by using the IEFPCM method [1, 3, 4]. After optimization, ^{15}N NMR chemical shift (δ_N) and coupling constants ($^{1}J_{CH}$) were calculated using the GIAO method [1, 3, 4] in methanol at the B3LYP/6-311++G(d,p)//6-31G(d) level under the keyword nmr = spinspin. Relative chemical shift was then estimated by using the corresponding formamide shielding calculated in advance at the same theoretical level as the reference. All the calculations were performed by using Gaussian 09 program package on a personal computer [8].

4. RESULTS AND DISCUSSION

The optimized molecular structure of 4-Chpy is presented in Figure 1. All the experimental values for $^{1}J_{CH}$ coupling constants of title molecule are given in Table 1. Substituents and hybridization of the carbon atom have crucial effects on C-H coupling constants. 4-Chpy molecule is good example to see those effects.

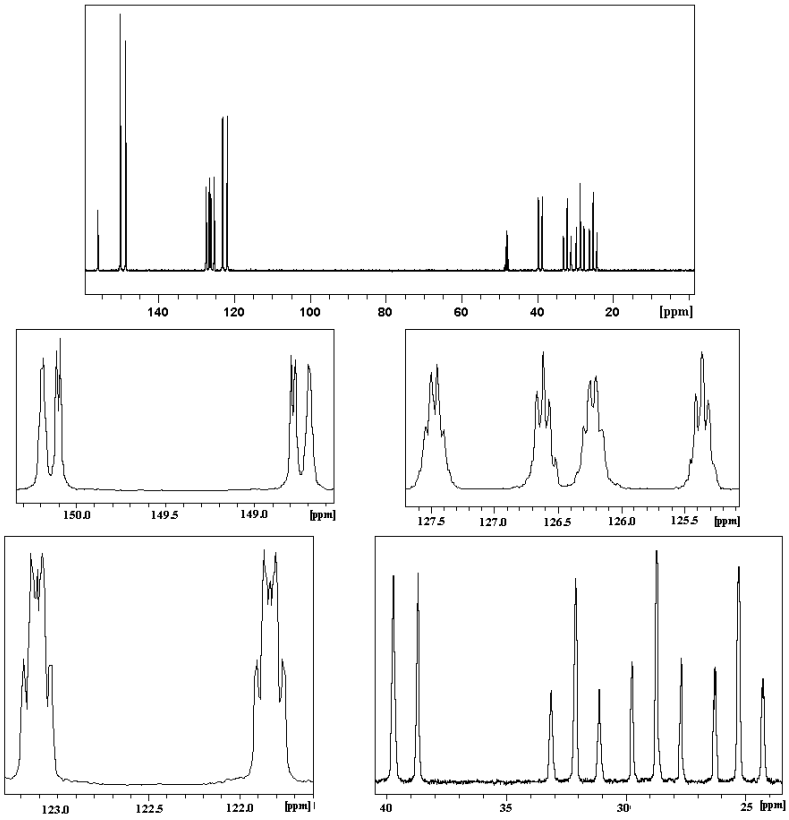

Fig. 2. Proton coupled ^{13}C NMR spectrum of 4-Chpy.

All the experimental and theoretical investigations for nitrogen atom were performed relative to formamide (δ = 112ppm, downfield of liquid ammonia) [9]. ^{15}N NMR spectrum of the title molecule is given in Fig. 3. The calculated and experimental ^{15}N chemical shift values of 4-Chpy are 202.35 ppm and 192.14 ppm, respectively.

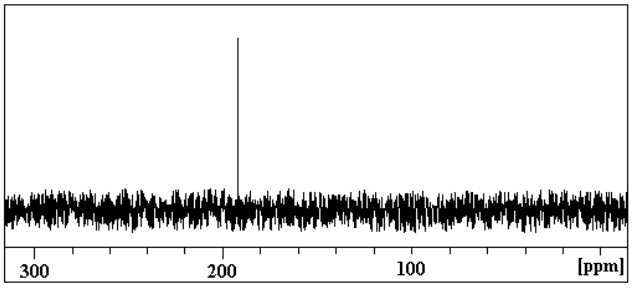

Fig. 3. ^{15}N NMR spectrum of 4-Chpy.

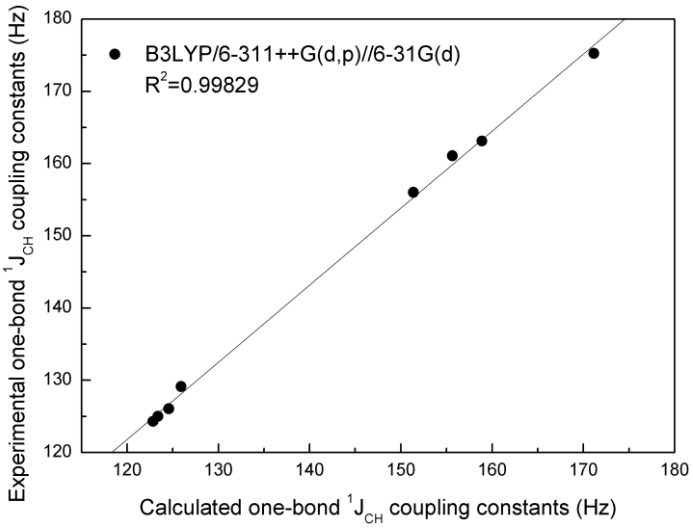

Fig. 4. Plot of the calculated vs. experimental $^{1}J_{CH}$ coupling constants of 4-Chpy.

5. CONCLUSION

The experimental and theoretical investigations of 4-Chpy molecule have been performed successfully by using NMR and quantum chemical calculations. Moreover, hybridization and type of the bond effects on $^{1}J_{CH}$ coupling constants for title molecule have been clearly observed in present study. For all calculations, it is shown that the results of B3LYP method are excellent agreement with all the experimental data.

[1] *C. Parlak, Ö. Alver, M. Şenyel,* ‘‘Experimental and theoretical NMR study of 4-(3-cyclohexen-1-yl)pyridine’’ Spectrochim. Acta A 69 (2008) 1252-1256.

[2] *Ş. Şentürk, C. Parlak, M.T. Aytekin, M. Şenyel,* ‘‘FT-IR spectroscopic study on some 4-(3-Cyclohexen-1-yl)pyridine metal(II) tetracyano-nickelate complexes’’ Z. Naturforsch. A 60 (2005) 532-536.

[3] *Ö. Alver, C. Parlak, M. Şenyel,* ‘‘FT-IR and NMR investigation of 1-phenylpiperazine: A combined experimental and theoretical study’’ Spectrochim. Acta A 67 (2007) 793-801.

[4] *Ö. Alver, C. Parlak, M. Şenyel,* ‘‘^{1}H, ^{13}C NMR and $^{n}J_{CH}$ coupling constants investigation of 4-Phenylpyridine: A combined experimental and theoretical study’’ Physics Lett. A 371 (2007) 300-306.

[5] *T. Helgaker, M. Jaszunski, K. Ruud,* ‘‘Ab initio methods for the calculation of NMR shielding and indirect spin−spin coupling constants, Chem. Rev. 99 (1999) 293-352.

[6] *Bagno, F. Rastrelli, G. Saielli,* ‘‘Predicting ^{13}C NMR spectra by DFT calculations, J. Phys. Chem. A 107 (2003) 9964-9973.

[7] *G. Bifulco, C. Bassarello, R. Riccio, L.G. Paloma,* ‘‘Quantum mechanical calculations of NMR j-coupling values in the determination of relative configuration in organic compounds, Org. Lett. 6 (2004) 1025-1028.

[8] *M.J. Frisch, G.W. Trucks, H.B. Schlegel, G.E. Scuseria, M.A. Robb, J.R. Cheeseman, G. Scalmani, V. Barone, B. Mennucci, G.A. Petersson, H. Nakatsuji, M. Caricato, X. Li, H.P. Hratchian, A. F. Izmaylov, J. Bloino, G. Zheng, J. L. Sonnenberg, M. Hada, M. Ehara, K. Toyota, R. Fukuda, J. Hasegawa, M. Ishida, T. Nakajima, Y. Honda, O. Kitao, H. Nakai, T. Vreven, J.A. Montgomery, Jr., J.E. Peralta, F. Ogliaro, M. Bearpark, J.J. Heyd, E. Brothers, K.N. Kudin, V.N. Staroverov, R. Kobayashi, J. Normand, K. Raghavachari, A. Rendell, J.C. Burant, S.S. Iyengar, J. Tomasi, M. Cossi, N. Rega, J.M. Millam, M. Klene, J. E. Knox, J. B. Cross, V. Bakken, C. Adamo, J. Jaramillo, R. Gomperts, R. E. Stratmann, O. Yazyev, A.J. Austin, R. Cammi, C. Pomelli, J.W. Ochterski, R.L. Martin, K. Morokuma, V.G. Zakrzewski, G.A. Voth, P. Salvador, J.J. Dannenberg, S. Dapprich, A.D. Daniels, Ö. Farkas, J.B. Foresman, J.V. Ortiz, J. Cioslowski and D.J. Fox.* Gaussian 09, Revision A.1, Gaussian Inc., Wallingford CT, 2009.

[9] *G.E. Martin, C.E. Hadden,* ‘‘Long-range 1H–^{15}N heteronuclear shift correlation at natural abundance’’ J. Nat. Prod. 63 (2000) 543-585.

Received: 12.12.2011

STRUCTURE AND ELECTRICAL PROPERTIES OF DOPED $TlGaSe_2$ AND $TlInS_2$ SINGLE CRYSTALS

SABAH ABED DAWOOD[a], ALEXANDER K. FEDOTOV[a], TOFIG G. MAMMADOV[b], ARZU I. NADJAFOV[b], MARIYA I. TARASIK[a]

[a]Belarusian State University, Independence av.4, 220030 Minsk, Belarus

[b]Institute of Physics of Azerbaijan National Academy of Science, Baku, Azerbaijan

In the doped crystals $TlGaSe_2$ and $TlInS_2$, using method of temperature dependencies of DC resistance in the temperature range of 100 – 300 K, the phase transitions at the temperatures of 240-245 K и 105-120 K were observed. The AC conductance measurements at room temperature indicated the hopping mechanism of carrier transport in the studied samples.

Keywords: layered crystals, phase transition, DC resistance, AC conductance
PACS: 61.66.Fn; 72.20.-I; 61.72.uf; 61.72.uj; 77.80.B; 61.44.F

INTRODUCTION

The ternary compounds $TlGaSe_2$ and $TlInS_2$ belong to the group of chalcogenide semiconductor crystals with layered structure which are crystallized in the same monoclinic structure. These crystals have received a great deal of attention due to their optical and electrical properties in view of the possible optoelectronic device application. In recent years there is a growing interest to their study due to the coexistence of ferroelectric and semiconductor properties, as well as the presence of structural phase transformations in some of these compounds. In particular, it has been established that, on cooling, some of undoped $TlGaSe_2$ and $TlInS_2$ crystals exhibit a sequence of structural phase transitions which accompanied by peculiarities on temperature dependencies of different properties: dielectric, elastic, acoustic, thermal, optical, etc., at temperatures ranges of ~ 90 – 140 K and ~ 242-253K for $TlGaSe_2$ and ~ 190-195 K and ~ 201-216K in $TlInS_2$ [1-6]. In spite of all these experimental results a complete conception about the reasons of these phase transitions has not been formed yet. Moreover it was interested to check the influence of doping on electrical properties and phase transitions in these crystals.

The present paper is devoted to the study of the surface structure and some electrical properties, including carrier transport mechanisms, at different temperatures in $TlGaSe_2$ and $TlInS_2$ crystals doped with different electrically active impurities.

EXPERIMENTAL

The single crystals were grown and doped with Fe, Ag, B, Tb, Er and Al impurities in evacuated quartz tubes by using the modified Bridgman method. The studied samples, which were in rectangular form, were oriented along the polar axis which lies in the cleavage plane (the morphology of crystals permits cleavage to plane parallel plates).

SEM investigations of the grown single crystals were done using LEO1455-VP scanning electron microscope with energie-dispersive Si:Li detector Rontec allowing to perform X-Ray microanalysis for checking the samples` stoichiometry.

DC resistance *R(T)* was measured in the temperature range 10 – 300 K using a closed-cycle cryogen-free cryostat system CFM (Cryogenic Ltd., London) and Lakeshore Temperature Controller Model 331, which allowed to scan the temperature with a rate of about 0.1-1 K/min and to stabilize the temperature with accuracy 0.005 K. The measurements of real part of AC conductance *G*(*f*) were performed at 300 K for the frequencies *f* between 100 Hz and 30 MHz using Agilent RCR Meters 4980A and 42841A. All electric measurements were carried out with full computer control.

For electrical measurements the wide face of plates were gently polished, cleaned and covered with two indium probes, which were applied by ultrasound soldering, so that the measuring current carried along the plane of the best split (normally to C axis).

RESULTS AND DISCUSSION

SEM investigations of single crystals confirmed their stoichiometry and have shown that surfaces of their normally-spaced faces displayed layered-like structure with piramid-like roughnesses of about 1 μm (Fig. 1).

The doping of crystals resulted in the lowering of their resistivity as compared to undoped ones that allowed to study DC conductance below 300 K and also AC conductance in a wide range of frequencies.

In order to get additional information about the mechanism of carrier transport and the succession of phase transformations in the doped $TlGaSe_2$ and $TlInS_2$ crystals, the temperature dependencies of the DC resistance in the above mentioned temperature regions were measured. The examples of *R{T}* dependencies in cooling regimes for the samples of doped $TlGaSe_2$<Fe> and $TlInS_2$<B> crystals are presented in Fig. 2.

The doping of crystals resulted in the lowering of their resistivity as compared to undoped ones that allowed to study DC conductance below 300 K and also AC conductance in a wide range of frequencies.

In order to get additional information about the mechanism of carrier transport and the succession of phase transformations in the doped $TlGaSe_2$ and $TlInS_2$ crystals, the temperature dependencies of the DC resistance in the above mentioned temperature regions were measured. The examples of *R{T}* dependencies in cooling regimes for the samples of doped $TlGaSe_2$<Fe> and $TlInS_2$<B> crystals are presented in Fig. 2.

As is seen, these measurements allowed to note a step-like peculiarity at T ≈ 240-245 K (marked with

arrows in figures). In addition, for $TlGaSe_2$<Fe> sample a low-temperature peculiarity (between 105 and 120 K) in shape of resistance oscillations was also displayed. Note, that similar phase transitions were observed in [5,6] by permittivity and thermal expansion coefficient temperature scanning in undoped $TlGaSe_2$ crystals.

Re-scaling of *R(T)* curves as Arhenius plots for T > 250 K (Insert (a) in Fig. 3) and for T < 105 K (Insert (b) in Fig. 3a) allowed to separate high- and low-temperature linear parts of ln*R* (1/*T*) dependencies with activation energies of about 0.25 eV and 0.04 eV correspondingly for $TlGaSe_2$<Fe> and 0.21 eV for $TlInS_2$<B> near the room temperature. For $TlInS_2$<Tb> and $TlInS_2$<Er> crystals linear parts in ln*R* - (1/*T*) curves near room temperature have given activation energies of conductance of about 0.17 and 0.14 eV appropriately.

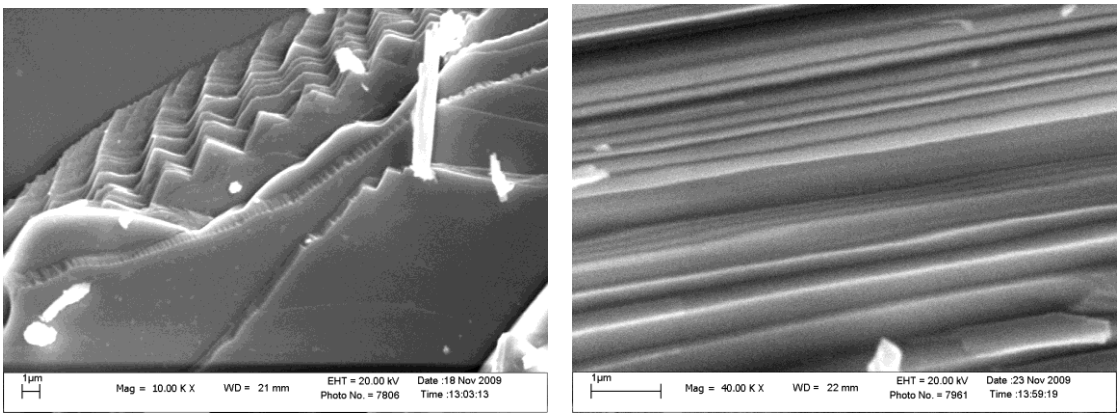

(a) (b)

Fig. 1. Examples of layered structures of the surface of $TlGaSe_2$ (a) and $TlInS_2$ (b) crystals doped with Fe and Ag properly.

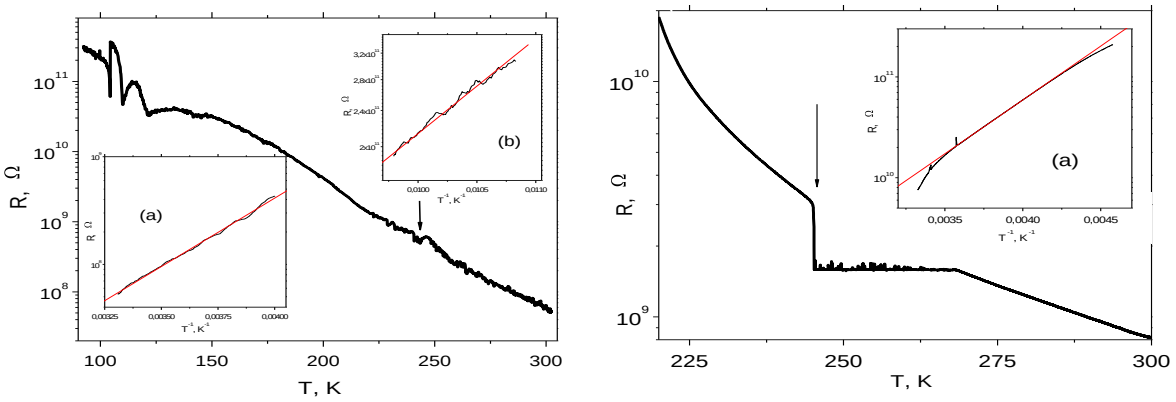

(a) (b)

Fig. 2. Temperature dependencies of DC resistance *R(T)* for $TlGaSe_2$<Fe> (a) and $TlInS_2$<B> (b) crystals measured in cooling down regime. Inserts present *R(T)* in Arhenius scale for T > 250 K (a) and for T < 105 K(b).

In order to additionally clarify carrier transport mechanisms in the studied crystals under doping we have studied the frequency dependencies of real part of AC conductance *G(f)* at room temperature. It was observed that the conductance increases with increasing frequency which is a normal trend for ferroelectric materials [7]. Presentation of *G(f)* dependencies in double logarithmic scale in Fig. 3 shows that for the most samples in the lowest and highest frequencies *G(f)* revealed power-like laws

$$G(f) \sim f^{\alpha}, \qquad (1)$$

with linear parts of lg *G* vs lg *f* that is characteristic for AC hopping mechanism of carrier transport [8]. Note that in $TlGaSe_2$ crystals in the intermediate frequency ranges *G(f)* curves displays sigmoid-like shape that corresponds to AC hopping model described in [9, 10]. The exponent α values (estimated by the slopes of linearized parts of *G(f)* curves) in Eq. (1) are strongly dependent on the frequency range and type of doping impurity. As is seen from Table 1, α values are changing from 0.11 to 1.04. In accordance with the model [9, 10], this is characteristic for hopping of electrons localized in the potential wells which representing the defects (impurities) in our case. After a jump of the electron from one neutral well to another one, the electrical dipole appears, so that the electron remains in the second well during the time τ and only then either jumps to the next (third) well, depending on the direction of the external electric field, with the probability *p*, or returns to the first well with the probability (1-*p*).

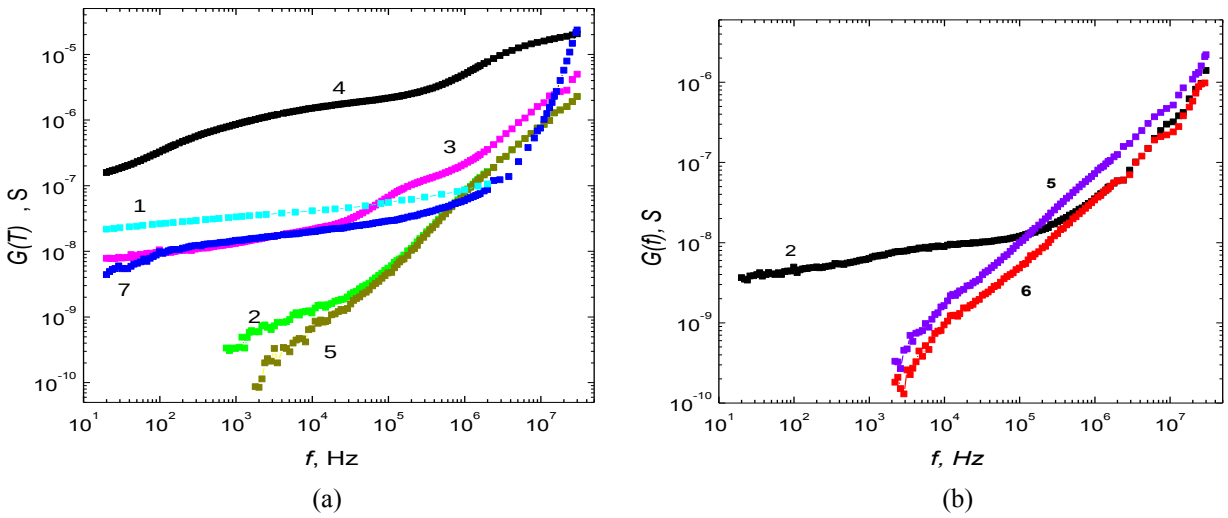

(a) (b)

Fig. 3. Frequency dependencies of real part of AC conductance *G(f)* at 300 K for $TlGaSe_2$ (a) and $TlInS_2$ (b) crystals doped with Fe (1), B (2), Al (3), Ag (4), Tb (5), Er (6) and Nd (7).

Table 1.

The α values in equation (1) for doped crystals $TlGaSe_2$ and $TlInS_2$ at low and high frequencies.

Doping element	Fe	B	Al	Ag	Tb	Er	Nd
$TlGaSe_2$							
α (10^2 <ω<10^4 Hz	0,11	0,85	0,14	0,42	0,13	-	0,14
α 10^5<ω<10^7 Hz	-	0,97	0,13	0,30	0,13	-	1.30
$TlInS_2$							
α (10^2 <ω<10^4 Hz	-	0.12	-	-	0,70	0.82	-
α 10^5<ω<10^7 Hz	-	0,92	-	-	0,87	1.04	-

Interaction of electrons in two neighboring potential wells leads to the certain distribution $F(\tau)$ of the probability p for the time τ. The model developed in [9, 10] allows to estimate the values of p and τ using the experimental $G(f)$ curves, relation (4) in [10]

$$p = G(f\to 0)/2G(f\to\infty)$$

and a model dependence of $\alpha(f)$, involved in the relation (1). In accordance with this model, $\alpha(f)$ dependence, which determines hopping probability p, has the shape of the curve with maximum at $f = f_{max}$ (see, Fig. 1 in [10]). As was shown in [9], f_{max} is connected with τ by the relation $\tau = 1/2\pi f_{max}$.

The analysis carried out in accordance with the model [9, 10] have shown that the hopping carrier transport in the most studied crystals is provided by, at least, two types of potential wells (defects). This is manifested, in particular, in two different slopes (α values) in *G(f)* curves shown in Fig. 3 (see, also Table 1) for $TlGaSe_2$ (curves 3,4,7) and $TlInS_2$ (curve 2) samples.

RESUME

In the doped crystals $TlGaSe_2$ and $TlInS_2$, using method of temperature dependencies of DC resistivity in the temperature range of 77 – 300 K, the phase transitions at the temperatures of the order of 240 K и 105-120 K were observed. The AC conductance measurements at room temperature indicate the hopping mechanism of carrier transport which is described by the model developed in our earlier works [9, 10].

ACKNOWLEDGMENTS

The work was partially supported by the VISBY Program of the Swedish Institute and Belarusian Fundamental Research Foundation by Contracts № Ф09Az-006

[1] *A. M. Panich,* J. Phys. Condenced Matter **20**, 3-31 (2008).

[2] *E. Şenturk, L. Tumbek, F. Salehli, and F. A. Mikailov*, Cryst. Res. Technol. **40**, , 248 – 252 (2005)

[3] *F.A. Mikailov, E. Basaran, T.G. Mammadov, M.Yu. Seyidov, E. ,Senturk*, Physica B **334**, 13–20 (2003)

[4] *F.A. Mikailov, E. Basaran, E. S. Entu, L.Tu. Mbek, T.G. Mammadov and V.P. Aliev*, Phase Transitions **76**, 1057–1064 (2003).

[5] *T. G. Mammadov1 and R. A. Suleymanov*, Phys. Stat. Solidi (b) **242**, 983–989 (2005)],
[6] *H. Yu. Seyidov and R. A. Suleymanov*, Soviet Solid State Physics **50**, 1169-1176 (2008).
[7] *C. K. Suman, K. Prasad, and R. N. P. Choudhary*, Materials, Chemistry and Physics **82**, 140–144 (2003).
[8] *Mott, N. F. & Davis, E.A.* Electronic Processes in Non-crystalline Materials, 2nd edn, Oxford Univ. Press, Oxford, 1979.
[9] *P. Żukowski, T. Kołtunowicz, J. Partyka, Yu.A. Fedotova, A.V. Larkin,* Vacuum **83**, S280-S283 (2009).
[10] *P. Zukowski, T. Kołtunowicz, J. Partyka, P. Wegierek, F.F. Komarov, A.M. Mironov, N. Butkievith, D. Freik,* Vacuum **81**, 11371140 (2007).

Received: 19.10.2011

THERMAL CHARACTERISTICS OF POLYPROPILENE FILMS WITH ADDITION OF Dk_2(10-40%) NANOGEL

M.A RAMAZANOV[1], R.L. MAMEDOVA, R.B. ASLANOV, A.A. KHADIYEVA, A.R. SADIKHOVA

[1]G.M. Abdullayev Institute of Physics of Azerbaijan NAS
AZ-1143, H.Javid ave., 33,
BSU, Baku, Z. Khalilov str., 23, Azerbaijan

The derivatograms of pure polypropylene (PP) and its mixture with nanogel volume content 10, 20 and 40 vol.% are presented. The nanogel addition in PP leads to total amorphisation of matrix crystalline phase, as the result of which the endothermal effects corresponding to the melting disappear on DTA curves. Note that exothermal effects on DTA curves in 210-310^{0}C interval are caused by thermal-oxidative destruction; the endoeffects at 275-290^{0}C are connected with break processes of weak bonds and endoeffects at 390-465^{0}C are connected with depolimerization processes. The nanogel particles in the quantity 20 vol.% influence very significantly that probably is connected with PP matrix crystalline part.

Keywords: Polypropylene, nanogel, thermal characteristics, derivatogram.
PACS: 79.60.Dp; 78.66.Li; 78.30.Am

INTRODUCTION

It is known that the use of different polymer material modification methods leads to significant expansion of their field application. Moreover, the directed structure change and polymer properties are carried out either in synthesis process or by the influence on the ready product by the introduction of another chemical nature fragments into macromolecule. Last time at the creation of polymer materials with the given properties, the modification of their surface is paid the special attention, as especially the surface layer structure mainly defines their behavior in operating conditions [1-4].

It is known that aging of polymer and its composites is connected with high local anisotropy of force field, caused by strong force difference of intramolecular and intermolecular interaction. From theory of heat properties of polymers and composites on its base follows that the presence of local anisotropy and conservation of macromolecule individuality in polymer compositional systems are able to lead to appearance of heat capacity specific regularities, negative coefficients of thermal expansion and series of another abilities.

It is mentioned in literature the fact that DTA can be express-method of organic synthesis allowing the revealing the substance behavior in wide temperature interval with the minimal use of portions and the definition of optimal temperature interval of process carrying in the case of their intra- and intermolecular interaction [5]. Earlier we have been studied the PP films treated by electrothermopolarization action filled by MnO_2 in quantity 0,5 and 1 vol.%. At influence of electrothermopolarization E=7·10^{6}V/m as the result of aging the amorphisation of PP matrix crystalline part occurs and because of that the thermostability decreases on 40°C in the comparison with PP which isn't treated by electrothermopolarization. It is established that electric field action leads to both total amorphization of PP+0,5vol.%MnO_2 composition and total depolymerisation accompanying by evaporation of formed intermediate products in quantity 100% [6]. Taking into consideration this fact the PP+D_{k2} samples are not treated by polarization.

Thermal characteristics of PP films with addition D_{k2}(10-40%) nanogel are investigated in the present paper. The powder mixtures of PP, D_{k1} and D_{k2} in different component ratios are prepared, further the nanocomposites PP+D_{k1} and PP+D_{k2} in the film form with further cooling are prepared from these mixtures by the method of hot pressing at melting temperature of polymer matrix at pressure 15MPa during 15 minutes. The samples are obtained in different temperature-time crystallization modes and especially, at slow cooling (SC) when samples are cooled up to room temperature with velocity 2 grad/minh and rapid cooling (RC) in the ice-water mixture with velocity 30 deg/min. RC samples are investigated by us.

The derivatograms are taken on G-derivatograf of "MOM" firm (Hungary) in temperature interval 20-500^{0}C in platinum crucible with heating velocity 5deg/min. The sensitivity by channels: DTA is 1/5; DTG is 1/15mg- 200. Al_2O_3 is used in the capacity of inert material at 1000^{0}C calcination during 24 hours [7].

The derivatograms of pure PP and its mixture with nanogel volume content 10, 20 and 40vol% : В С, Д correspondingly, are presented on fig.1. The changes of PP thermal characteristics after filling are presented in the table. According these data after nanogel turn from 10 up to 40vol.% on DTA curves, the following changes are observed: 1) beginning the introduction from 10vol.% nanogel in PP the amorphization of PP matrix crystalline part takes place; 2) the beginning of thermo-oxidative destruction temperature decreases up to 210^{0}C with increase of nanogel concentration up to 40vol.%, the bond breakage at 270^{0}C, the depolymerization at 370^{0}C. These data in initial PP are observed at T = 230^{0}C, 318^{0}C and 465^{0}C correspondingly. As it follows from above mentioned data the nanogel addition in PP leads to total amorphization of matrix crystalline phase as the result of which the endothermal effects corresponding to

melting disappear on DTA curves, i.e. the total amorphization of matrix crystalline phase takes place. The data analysis on DTA, ДТG and TG curves allows us to conclude that amorphization of PP crystalline part is caused by polymer structural changes on molecular and permolecular levels existing under influence of nanogel addition particles. Thermal characteristics of PP+20vol% nanogel mixture strongly differ from another ones (fig.1, C).

The decrease of temperature of thermo-oxidative destruction beginning up to 210^{0}C (see table), temperature of bond breakage up to 270^{0}C and depolymerization up to 380^{0}C, bond breakage up to 230^{0}C is connected with the fact that all nanogel particles destroy the crystallization centers of PP matrix crystalline phase and occur the total crystal amorphization. Probably, in amnorphization process the crystal dropping to matrix amorphous part takes place and the PP amorphous part is enriched. Note that exothermal effects on DTA curves (fig. 1 A,B,C,D) in interval 210-310^{0}C are caused by thermo-oxidative destruction. The endoeffects at 275-290^{0}C are connected with processes of weak bond breakage, endoeffects at 390-465^{0}C are connected with depolymerization processes.

Thus, the nanogel disperse particles on PP structure all levels leads to total amorphization of filled material. The most significant influence on these properties has the nanogel particles in quantity 20 vol.% that probably is connected with crystalline part of PP matrix .

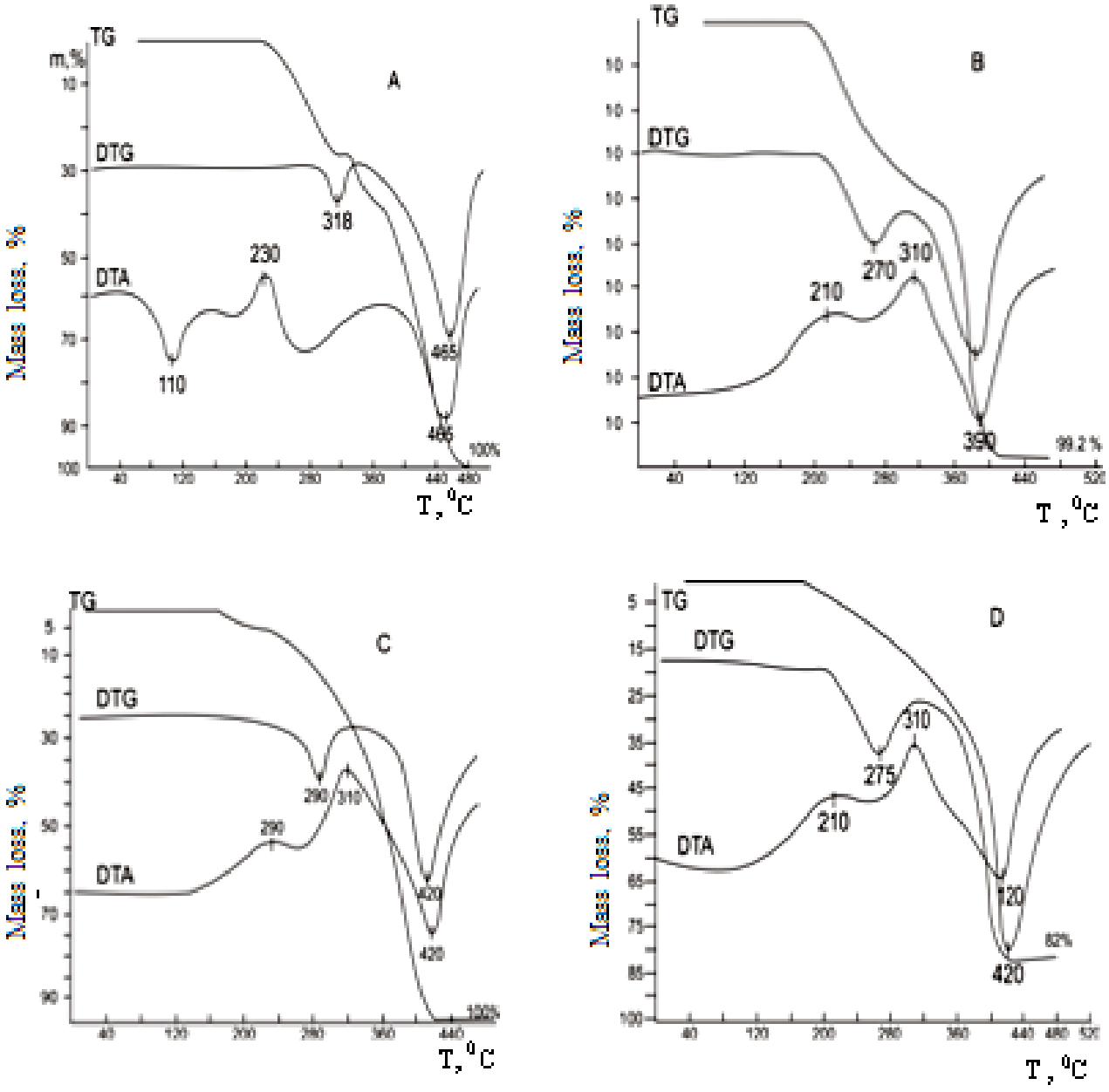

Fig. 1. Derivatograms of PP films with nano-gel addition: A) initial PP, B) PP+10%, C)PP+20%, D)PP+40% of nanogel.

Table.

Thermal characteristics PP films with addition of Dk_2(10-40%) nanogel

Material	Tcr. ^{0}C	K,%	Td, ^{0}C	Tb, ^{0}C	Tdep, ^{0}C
PP pure	110	48	230	318	465
PP+10%nanogel	-	-	210	270	390
PP+20%nanogel	-	-	290	310	420
PP+30%nanogel	-	-	240	310	410
PP+40%nanogel	-	-	210	275	420

Notes: Tcr is crystal melting temperature;
K is crystallinity degree;
Td is temperature of thermo-oxidative destruction beginning;
Tb is temperature of bond breakage;
Tdep is depolymerization temperature.

[1] *N.A. Eyubova, A.M. Maqerramov, V.P. Malin, Yu.N. Qazaryan.* Issledovanie elektrichrskogo stareniya plenki polietilena derivatograficheskim metodom.V sb.: Radiaciya v fizike i ximii. Baku, Elm, vip1, s.9-13. (In Russian).

[2] *M.A. Baqirov, N.A. Eyubova, V.P. Malin, A.A. Aliev, A.M. Maqerramov.* Vliyanie elektricheskoqo stareniya na kristallichnost polimernix dielektrikov. Visokomolek. soed, M, 1987,t. 29A, №5, s.917-919. (In Russian).

[3] *I.Yu. Apalikova, Yu.I. Suxarev, T.Q. Krupnova.* Derivatoqraficheskie issledovaniya oksiqidratov jeleza (III), poluchenn;x applikachionniem metedom. Yujno-Uralskiy qosudarsstvenniy universitet., q. Chelyabinsk, Rossiya.(In Russian).

[4] *V.I. Povstuqar, V.I. Kodalov, S.S. Mixaylova.* Starenie I svoystva poverxnosti polimernnix materialov. M., 1988. (In Russian).

[5] *A.S. Kozlov, S.B. Piraqov, I.B. Chelinskiy.* Sankt-Peterburg,1980, 13.(In Russian).

[6] *M.A Ramazanov, A.S. Quseynova, N.A. Eyubova* Optoelectronics and advanced materials-Rapid communications. Ruminiya. Vol.5, №4, April 2011, p 410-413

[7] *V.S. Qorshkov, B.B. Timashev, B.Q. Savelev.* Metodi fiziko-ximicheskoqo analiza vyajushix veshestv. M.:Visshaya shkola, 1981 s.37-42.(In Russian).

Received: 14.10.2012

THE PECULIARITIES OF SCATTERING MECHANISM OF CHARGE CARRIERS IN SOLID SOLUTIONS $Bi_{1-x}Sb_x$ (x=0,3;0,75) AT T=77K

B.A. TAIROV, V.A. ABDURAKHMANOVA, H.A.GASANOVA, M.A. ASLANOV
G.M. Abdullayev Institute of Physics of Azerbaijan NAS
AZ-1143, H.Javid ave., 33

The investigations of resistivity ρ, Hall coefficient R and magnetic resistivity $\Delta\rho/H^2$ in $Bi_{1-x}Sb_x$ ($x=0,3;0,7$) polycrystals at temperature $77K$ are carried out.

It is shown that change of electron mobility in the dependence on alloy composition $Bi_{1-x}Sb_x$ at $T=77K$ is explained by of charge carriers on acoustic branch of lattice oscillation spectrum and alloy disorders.

Keywords: scattering mechanism, solid solution, charge carriers
PACS: 64.75.Nx; 72.20.Pa

INTRODUCTION

During last several years the interest to bismuth and $Bi_{1-x}Sb_x$ alloy is increased [1-5]. The small value of heat conductivity and small one of electron effective mass in solid solutions $Bi_{1-x}Sb_x$ allows us to apply them in the gauges of IR radiation and thermoelectric generators the characteristics of which are indirectly connected with scattering mechanism of charge carriers. In spite of many investigations of Bi-Sb solid solutions, the scattering mechanism of charge carriers in this system at compositions close to equimolar one stays unclear. In the given ref the attempt of quantitative explanation of mobility change of charge carriers in the connection with scattering processes on alloy disorders and nonquadraticity of scattering law, is made.

As it is mentioned in [6], the homogeneous alloy single crystals Bi-Sb can be obtained with stibium content up to *30at%*. At big stibium content the single crystal obtaining is essentially difficult. That's why the investigations of solid solutions Bi-Sb with stibium content more than *30at%* are carried out on polycrystalline samples.

EXPERIMENTAL RESULTS AND DISCUSSION

The sample obtaining technique is described in [6]. The resistivity ρ, Hall coefficient R and magnetic resistance $\Delta\rho/H^2$ of solid solutions $Bi_{1-x}Sb_x$ ($0,3<x<0,7$) are measured. The values of these values in weak magnetic field at temperature $77K$ are given in table 1.

The calculation of Bi-Sb alloy main parameters is carried out by isotropic model which gives the good results at the evaluation of average mobilities of alloy polycrystals of Bi-Sb type, as it is mentioned in [7,8].

For definition of concentration and mobility of charge carriers the two-band isotropic model allowing the definition of concentration and average mobilities, is used:

$$\frac{1}{\rho} = eN\mu\left(\frac{1}{b} + 1\right) \qquad (1)$$

$$R = \frac{1}{eN}\frac{b-1}{b+1} \qquad (2)$$

$$\frac{\rho_\Delta\,\rho}{RH^2} = \frac{b}{(b-1)^2} \qquad (3)$$

The calculated values of mobilities of electrons and holes and also their concentration ($N_э=N_d=N$) are given in table 2. As it is seen from the table, the relation of mobilities of electrons and holes in Bi-Sb alloys gradually decreases with increase of stibium content striving to unit. Such mobility relation change is corresponded with the known fact from literature, i.e. Hall coefficient sign in alloys containing *70-80at%*Sb [9,10].

The mobilities of electrons and holes decrease with increase of stibium content in Bi-Sb alloys. The last one, as it is shown below, is connected with growth of charge carrier concentration, leading to increase of effective mass because of scattering law nonquadraticity and also with increase of scattering of current carriers.

Note that the electron effective mass is the energy function in bismuth, stibium and obviously, in bismuth-stibium alloys under scattering law nonquadraticity. The nonquadraticity of energy dependence on quazi-impulse, as it is known, becomes the significant, when energy gap between bands is comparable with electron energy. In bismuth, in particle, the valence band being below on *0,015ev* than its bottom corresponds to conduction band minimums in L point. By other hand, electron energy in bismuth is equal to *~0,03eV*. The interaction of nearest bands is usually taken under consideration in zero approximation of *kp*-perturbation theory [11].

Table 1
The dependence of specific resistance, Hall coefficient and magnetic resistance on alloy composition. Bi-Sb, $T=77^0K$

Alloy composition	$\rho\cdot10^4$ ohm·cm	R, $cm^3\cdot C^{-1}$	$\Delta\rho/H^2\cdot10^{11}$ ohm ·cm/oe^2
Bi_{65} Sb_{35}	1	2,69	5,17
Bi_{60} Sb_{40}	0,9	1,92	2,99
Bi_{55} Sb_{45}	0,8	1,52	2,56
Bi_{50} Sb_{50}	0,75	0,61	0,86
Bi_{45} Sb_{55}	0,7	0,326	0,35
Bi_{40} Sb_{60}	0,53	0,114	0,17

Firstly, such calculation was carried out in Kein [12] applicable to JnSb. In Kein model, however, extremums are located in point *k=0* and electron isoenergetic surfaces in zero approximation of excitation theory are spheric ones. The contribution relatively remote band in more high approximations of excitation theory is also taken under consideration in Kein theory. In semi-metals of VB-group and their solid solutions the isoenergetic surface form is far from spheric one, that's why Kein model generalized for the case of Fermi ellipsoidal surfaces can be used for taking under consideration scattering law nonquadraticity [13]. In this case one can suggest that both transversal and longitudinal effective masses of electrons and holes are defined by the electron interaction of nearest valence and conduction bands.

Table 2

The change of electric parameters of Bi-Sb alloys on the composition, $T=77^0K$

Alloy composition	b	$N\cdot10^{-3}$ cm^{-3}	$\nu\cdot10^{-4}$ $cm^2/\mathbf{V}\cdot sec$	$\mu\cdot10^{-4}$ $cm^2/\mathbf{V}\cdot sec$
Bi_{65} Sb_{35}	1,45	4,28	5,96	8,67
Bi_{60} Sb_{40}	1,44	5,83	4,88	7,03
Bi_{55} Sb_{45}	1,40	6,84	4,75	6,65
Bi_{50} Sb_{50}	1,27	12,30	2,98	3,78
Bi_{45} Sb_{55}	1,23	19,63	2,04	2,51
Bi_{40} Sb_{60}	1,12	31,60	1,76	1,97

where $b=\mu/\nu$

The application of modified Kein model corresponds to suggestion about electrons with anisotropy coefficient independent on energy. The last one corresponds to similar change of state density effective mass on energy as in the case of Kein isotropic model.

In bismuth and especially in stibium, electron effective mass can be considered as significantly less one than free electron mass in direction of bisectrix axis. However, Kein model, as it is shown below, well describes the change of average mass on energy. In generated case for Kein model [14] the dependence of electron effective mass on current carrier concentration is defined by following expression [15]:

$$\left(\frac{P_0}{P}\right)^2 = 1 + \frac{2p_0h^2\,(3\pi^2\,n)^{\frac{2}{3}}}{m_0 8_g} \qquad (4)$$

$$P_0 = \frac{1}{m_0^*} - 1 \qquad (5)$$

$$P = \frac{1}{m^*} - 1 \qquad (6)$$

m_0 is free electron mass; m_0^*, m^* are given values of effective mass.

On the band bottom and at the given current carrier concentration, correspondingly: ε_g is gap between valence and conduction bands. In bismuth ε_g= 0,015eV.

Besides, electron effective mass in undoped bismuth is equal to ~0,04m_0 and on conduction band bottom ~0,0021 m_0, i.e. in expressions (5) and (6), unit in comparison with $\frac{1}{m_0^*}$ and $\frac{1}{m^*}$ can be ignored. Such expression (4) can be written in the form:

$$\left(\frac{m^*}{m_0^*}\right)^2 = 1 + \frac{2h^2\,(3\pi^2\,n)^{\frac{2}{3}}}{m_0^*\,m_0 8_g} \qquad (7)$$

Using this relation on known value electron effective mass [16] and current carrier concentration in undoped bismuth, one can define the effective mass on conduction band bottom. The calculation gives the value *0,0026* m_0, that well agrees with *0,0021* m_0 value calculated on experimental results [17]. The last one proves about application possibility of such simplified model for calculation of effective mass dependence on current carrier concentration in bismuth.

By other hand, in stibium the electro-wave energy spectrum is similar to one in bismuth. The difference between them obviously is defined by significantly bigger electron energy and change ε_g (according to [18] in stibium ε_g ≈ *0,1eV*).

For evaluation of electron effective mass in stibium the expression (7) can be simplified, taking under the consideration that second member in right part is significantly bigger than unity. Ignoring unity, we obtain:

$$m^* = \frac{\sqrt{2}m_0^{*\frac{1}{2}}h\,(3\pi^2\,n)^{\frac{1}{3}}}{m_0^{\frac{1}{2}}\,\varepsilon_g^{\frac{1}{2}}} \qquad (8)$$

Taking under the consideration the fact that effective mass on bottom band is approximately to ε_g, we obtain:

$$m^* = A\cdot n^{\frac{1}{3}} \qquad (9)$$

where *A* is the value not depending on charge carrier concentration.

The electron effective mass in stibium which is equal to ~*0,2*m_0 can easily defined by known value of effective masses of bismuth and stibium. This value agrees with effective mass value defined from cyclone resonance [19] if we take under consideration the error in the definition of carrier sign [20]. The last one proves about application possibility (9) for evaluation of changes of electron effective mass and Bi-Sb alloys.

For evaluation of electron mobility $(\frac{e\tau}{m^*})$ in Bi-Sb alloys is also necessary to know the change character of time relaxation on current carrier concentration.

The detail investigations of current carrier scattering mechanisms in bismuth, carrying in (22), show that at low temperatures it is necessary to take under the consideration also the intervalley scattering and scattering anelasticity. However, in this paper, it is shown that current carrier scattering at temperatures by 100^0 *K* order can be considered as elastic one. Besides the scattering on acoustic phonons, in semimetal alloys, the scattering on alloy disorders can be significant one.

Using the relations given in [23], we can show that relaxation time in generated case is proportional to $n^{-\frac{2}{3}}$ at electron scattering. That's why taking under consideration the effective mass dependence on charge carrier concentration, we can write:

$$\mu_{ac} = Bn^{-1} \tag{10}$$

where B coefficient is defined by charge carriers not depending on concentration. The definition of this coefficient is difficult because of unknown value of deformation potential. However, the comparison with experiment can be carried out on the dependence of charge carrier mobility on their concentration.

This change is weaker than n^{-1}.

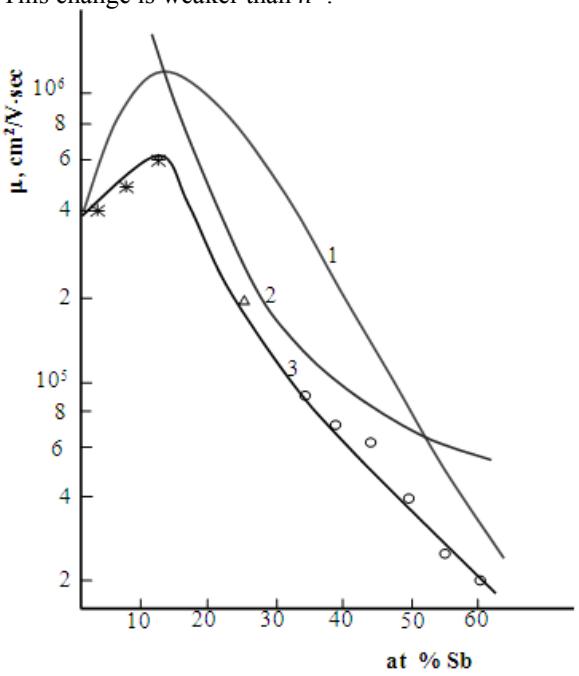

Fig. The dependences of electron mobilities in $Bi_{1-x}Sb_x$ alloys on alloy composition at *T=77K:* 1 is acoustic scattering; 2 is scattering on alloy disorders, 3 is total scattering.

The last one can be connected with additional scattering on alloy disorders. The relaxation time is defined by relation [24] at scattering on alloy disorders:

$$\tau \approx \frac{c}{x(1-x)} \tag{11}$$

where x is atomic content of the one of components, and c depends on the difference in atomic weights of components and difference of atom bond energy in component lattices.

In obvious form the relations defining the c parameter aren't written.

The B parameter values in expression (10) and c parameter values in expression (11) are defined by two values of electron mobility in Bi-Sb alloys of different composition with taking under consideration the sum of reversal values of charge carrier mobility limited by separate scattering mechanisms:

$$\mu^{-1} = \mu_{ac}^{-1} + \mu_{disord}^{-1} \tag{12}$$

The electron mobility limited by limited by scattering on alloy disorders according to selection on experimental data is defined by relation:

$$\mu_{disord} = \frac{2.1\cdot10^{10}}{x(1-x)V} n^{1/3} cm^{-1}\cdot sec^{-1} \tag{13}$$

and the mobility limited by scattering on acoustic phonons.

$$\mu_{ac} = \frac{1.1\cdot10^{23}}{V} n^{-1} cm^{-1}\cdot sec^{-1} \tag{14}$$

The dependences of mobilities $\mu_{disord.}$ and $\mu_{ac.}$ on Bi-Sb alloy composition are showed on the figure (curve 1 and 2, correspondingly. The sum mobility is presented on curve 3).

As it is seen from the figure, the calculated dependence is satisfactory agreed with both our data and data of other authors in spite of far extrapolation of dependences. This can serves the evidence of above mentioned mechanism of electron scattering in Bi-Sb alloys.

Thus, it is shown in the present paper that the change of electron mobility on alloy composition Bi-Sb (at $T=77^0K$) can be calculated at taking under consideration the scattering law nonquadraticity and charge carrier scattering on spectrum acoustic branch of lattice oscillation and alloy disorders.

[1] *J. Luli, G. Checkelsky, Y.S. Hor, C. Uher, A.F. Hebard, R.İ. Cava, N.P. Ong.* Science journal, 321 № 5888 (2008) 547.

[2] *N.P. Ong, G. Luli, J. Josep, G. Checkelsky, R.İ. Cava.* Affiliation: Dept of Physics, [Link to ong Lab→]. Physics com (2008)

[3] *İ. Kerner.* Moldavian Journal of the Physical Sciences, 4№3 (2005)318.

[4] *G.N. Korhemyaki, M.A. Nalivkin, M.A. Rom, P.V. Mateychenko, J. Cryst.* Growth, 263 №4 (2004) 148

[5] *D.Sh. Abdinov, T.D. Alieva, N.M. Axundova, M.M. Taqiev.* Transactions of Azerbaijan Academy of Sciences, Series of Physical-mathematical and Technical Sciences, Physics and Astronomy, XXIII №5 (I) (2003) 41.

[6] *B.A. Tairov.* Dispersiya elektromaqnitnix maqnetoplazmennix voln i qalvanomaqnitnie effekti v splavax Bi_{1-x} Sb_x.Diss. na zvanie doktora fiz-mat.Nauk Baku (1994). (in Russian).

[7] *Q.A. Ivanov, A.M. Popov.* FTT, 1963, №5 (in Russian).

[8] *Q.A. Ivanov.* «Uc.Zap.LQPI im. Qercena, 265, 193,1965 (in Russian).

[9] *S.Tapuma.* J. Phys.soc. Japan, 16,2349, 1961.

[10] *B.T. Bibol, P.P. Bodyul, D.B. Qicu.* Fm.M. 23,937,1967. (in Russian).

[11] *Yu.I. Ravich, B.A. Efimova, I.A. Smirnov.* Metodi issledovaniya poluprovodnikov v

primenii k xalkoqenidam s vinca PbTe, PbSe, PbS, M.Izd-vo. «Nauka», 1968. (in Russian).
[12] *E.O. Kane.* Phys.Chem.Solids, 1,249,1956
[13] *J. Kolodziejcsak, L. Sosnovski.* Acta phys.Polon, 21,399,1962.
[14] *J. F. Koch and J.D. Jensen.* Phys.Rev,184,643,1969
[15] *B. Lax , J.G. Mavroides, H.J. Zeiger and R.J. Keyes.* Phys.Rev. Letters, 5, 241,1960
[16] *M.S. Dresselhaus and J.G. Mavroides.* Phys.Rev. Letters,14,259,1965
[17] *W.S. Datars and J. Vanderkooy.* JBM, J.Res Develop, 8, 247,1964
[18] *O. Octu and G.A. Saunders.* Proc. Phys.Soc, 91, 156,1967.
[19] *B.M. Mujdaba.* Kand. Diss. IPAN SSSR, L.1969.(in Russian).
[20] *B.M. Askerov.* Teoriya yavleniy perenosa v poluprovodnikah Baku. Izd-vo. A. N. Azerb . SSSR, 1963. (in Russian).
[21] *D. Zayman.* Elektroni i fononi M.1962. (in Russian).
[22] *A.A. Kuliev, M.Q. Shaxtaxtinskiy, D.S. Tomtiev.* «Izd. AN Azerb. SSR, seriya fiz-tex. i matem. Nauk» , 3, 17, 1967. (in Russian).
[23] *M. Ableles and S. Meiboon.* Phys. Rev. 101, 544, 1956.

Received: 14.11.2012

FORMATION OF CADMIUM SULPHIDE NANOPARTICLES BY ACOUSTOCHEMICAL METHOD

M.B. MURADOV, N.V. HUSEYNOVA*, E.H. KULIYEV, G.M. EYVAZOVA

Baku State University, AZ-1148, Z.Khalilov 23, Azerbaijan

**SOCAR SIC Nanotechnologies*

The cadmium sulphide nanoparticles are obtained by acoustochemical method and their structure and optical properties are investigated. It is shown that effective mass values in the obtained nanoparticles differ from ones in volume crystals of cadmium sulfide. Crystal structure of CdS nanoparticles depends on formation condition.

Keywords: crystal structure, nanoparticle, acoustochemical method
PACS: 78. 68. DOI: 10. 1134

The nanoparticles of chalcogenide semiconductors have the wide application perspectives in the the different fields of science and technology. They can be applied in optoelectronics [1], sun elements [2], cathalysis [3,4], in medicine as biomarkers [5] due to their unical properties.

It is known that physicochemical properties of nanomaterials depend on crystal structure sizes and geometry of formed materials. These material parameters strongly depend on methods of nanostructure formation. The conditions of nanomaterial formation can strongly influence on the structure, arrangement and the form of obtained materials. In [6] we show that the additional potential in nanostructures which forms because of nanomaterial defect structure, can strongly influence on nanostructure physicochemical properties. That's why the investigations of physicochemical properties in the dependence on the nanostructure formation condition are actual ones. The methods which allow us to control the nanomaterial properties are perspective ones for the further usage in industry. The several methods of obtaining of cadmium sulphide nanoparticles such as chemical evaporation from solutions [7,8], SILAR [9,10], sol-gel [11,12] and etc are known.

The obtaining of chalcogenide semiconductor nanoparticles by acoustochemical method [13-20] is the one of the perspective and simple one. In [21] the cadmium sulphide nanoparticles are obtained by ultrasonic processor with parameters ν = 23 kHz, P = 200 W. The obtained particles have the cubic modification with particle average size d ~ 5,8 nm. The time of ultrasonic machining is 60 minutes. The thiourea is used as the stabilizing agent.

In [22] CdS nanoparticles are obtained by acoustochemical method with the use of isopropyl alcohol in the capacity of stabilizing agent. The time of ultrasonic machining is ~3h. The particle structure is cubic one. The average particle size is ~3,3 nm.

In the given work the structure, morphology, optical parameters of nanoparticles are investigated on the example of cadmium sulphide ones; the comparable analysis of particle sizes defined by XRD and from calculations of the forbidden band width change because of quantum dimensional effect, is carried out.

TECHNOLOGY

The acoustochemical method is used for obtaining of CdS nanoparticles. $Na_2S_2O_3 \cdot 5H_2O$ and $CdCl_2 \cdot 2.5\ H_2O$ are dissolved in isopropyl alcohol and then the solution is solved by distillated water up to 100ml . The ultrasonic processor of VCX500 (20 KHz, 500 w) type is used for nanoparticle synthesis. The nitrogen is constantly fed to the bulb for oxygen extraction from the system.

The nitrogen running through the system purifies the solution from the dissolved oxygen and doesn't give the possibility to CdO formation because of reaction of oxygen and cadmium ions. Experiments carried out without nitrogen feeding to the system show that in this case the solution with dark-grey shadow forms in the volume that evidences about formation of cadmium oxide nano-particles. In order to exclude this process it is necessary to delete the dissolved oxygen from the system. Note that dissolved oxygen is present at the water and also forms in the system under the action of acoustic waves which mix the air with solution. The solution of isopropyl alcohol and distillated water containing $Na_2S_2O_3$ and $CdCl_2$ is treated by ultrasonic processor during 3 hours. The power of source is regulated on the 200kW level. After treatment the solution has the yellow color that evidences about formation of cadmium sulphide nanoparticles.

With the lapse of time CdS nanoparticles with big sizes precipitate on the bulb bottom. The solution upper layer, containing the particles with small sizes, is taken after one day. Further the isolated sample is put to centrifuge CNR-2060 and treated at 4000 rev/sec velocity. The isolated CdS nanoparticles are mixed with water solution of polyvinyl alcohol (PVS) and nanocomposites CdS/PVS are obtained.

RESULTS AND DISCUSSION

The structure of obtained cadmium sulphide nanoparticles is investigated by X-ray diffractometer (XRD diffractometer Bruker D8 ADVANCE). The diffractogram from CdS/PVS samples is shown on fig.1. As it is seen from the figure the nanoparticle structure is hexagonal one. The nanoparticle average size is defined by Debye-Scherrer formula[21]:

$$L=K\lambda/\beta\cos\theta \quad (1)$$

where L is crystallite size, λ is X-ray radiation wave length (λ=1.54A), K is constant which is equal to 0,94, β is peak half-width in radians, θ is peak diffraction angle. The calculations show that average size of CdS, defined by this formula, is 22,2m.

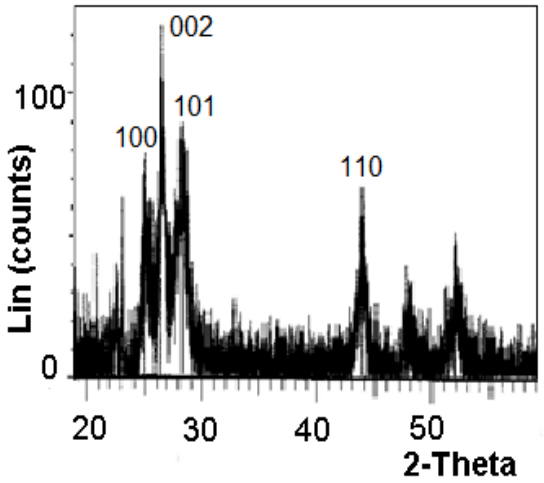

Fig. 1 Diffractogram of CdS/PVS nanocomposite

In [22, 18] the cadmium sulphide nanoparticles with cubic modification are obtained analogously by ultrasonic processor. Only in this case the power of uiltrasonic processor is 100W and frequency is 40kHz. The particle sizes are 3,3nm.

The investigation of [17-22] shows that there is no correlation between medium parameters (frequency and power) and structure of obtained nanoparticles. In [21] (v = 23kHz, P = 200W), [22] (v = 40kHz, P = 100W), [18] (v = 40kHz, P = 100W) the structures are cubic ones. In [17] (v = 20kHz, P = 60W), [20] (v = 23kHz, P = 200W) structures are hexagonal ones. In our experiments the radiation frequency v=20kHz, and radiation power P = 200W. It is known that formation temperature of hexagonal phase is higher than formation temperature of cubic one. However, in nano-systems the nanoparticle thermodynamic state can influence on stability of formed phase. The deposition into surface energy change can be taken from particle form and also the type of stabilizing agent.

The optical properties of obtained samples are investigated on UV-V is spectrophotometer SPECORD 250 of Analytic Jena firm. The transmission spectrums of CdS/PVS samples and $(\alpha h\nu)^2$ dependence on $(h\nu)$ photon energy are shown on *Fig.2*. As it is known, the absorption coefficient for straight-band semiconductors is defined as [23]

$$\alpha \sim (h\nu - Eg)^{1/2} \cdot \frac{1}{h\nu} \quad (2)$$

The forbidden bandwidth is defined on the basis of this dependence. The forbidden bandwidth is 3,62eV. It is known that the forbidden bandwidth depends on sizes in following way [24]:

$$E_g^{\,2} - E_{gb}^{\,2} = \frac{2\hbar^2 E_{gb}\pi^2}{2\mu d^2} \quad (3)$$

where E_g is forbidden band width for nano-particles, E_{gb} – for volume crystals, μ is effective dynamic mass of electrons and holes in nano-particles of cadmium sulfide, d is average size of nano-particles.

$$\mu = \frac{m_h m_e}{m_h + m_e} \quad (4)$$

where m_h is hole effective mass, m_e is electron effective mass. As it is mentioned in [23, 24], effective mass of electrons and holes in the particles should differ from effective mass in volume of crystals. The particle average size calculated on formula (3) is 1,39nm. Note that the values of effective mass of electrons and holes for cadmium sulfide crystals are used at calculation of particle sizes at the formula (4). The values of forbidden band width for volume crystals CdS is E_g = 2,42 eV [6].

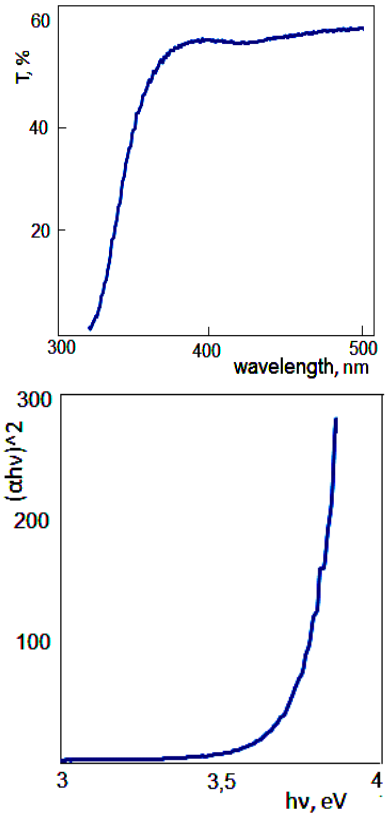

Fig. 2. The transmission spectra of CdS/PVS nanocomposite and the dependence $(\alpha h\nu)^2$ on photon energy

The values of particle average size, defined by Debye Scherrer formula, strongly differs from these values and is equal to 22,2nm. Obviously, this is connected with the difference of effective masses in crystals and nano-particles.

The value of effective dynamic mass of charge carriers in cadmium sulfide nano-particles is defined on the basis of particle sizes defined by X-ray diffraction and forbidden band width defined on the basis of optical spectra from formula (3). The calculated values of effective dynamic mass of charge carriers is μ = 0,001 that essentially differs from μ = 0,1556 value for volume crystals.

Thus, the cadmium sulfide nano-particles are obtained in the given ref by acoustochemical method, their structure and optical properties are investigated. It is shown that effective mass values in obtained nano-particles essentially differ from cadmium sulfide volume crystals. The crystalline structure of CdS nanoparticles depends on formation condition.

[1] *N. V. Hullavarad, S. S. Hullavarad*, Proceedings of 2009, Nanoelectronic Devices for Defense and Security, Paper 159, IV(A1) Optoelectronics Materials & Devices Session (2009)

[2] *R.S.Singh, V.K. Rangari, S.Sangapalli, V. Jayaraman, S. Mahendra, V.P. Singh* ,Solar energy materials & solar cells, 2004, 82, 315-33

[3] *S.Y. Ryu, J.Choi, W.Balcerski, T.K.Lee, M.R.Hoffmann*, *Industrial &* Engineering Chemistry Research, 2007, *46*, 7476

[4] *Ahed Zyoud; Nidal Zaatar; Iyad Saadeddin; Cheknane Ali; DaeHoon Park; Guy Campet; Hikmat S. Hilal,* J. Hazardous Mat., Elsevier, (25 August, 2009).

[5] *G. Jie , L. Wang , S. Zhang ,* Chemistry. 2011, 17 (2), 641-8

[6] *M.B. Muradov, G.M. Eyvazova, R. Turan , A.M.Maharramov* , J. Opt. Adv. Mat.-OPEN J-Gate-Worlds, 2008,Vol. 2, No. 12, p. 775 – 778

[7] *Hai-Ning Cui, Manuel F. Costa, V. Teixeira, Jun Zhang,* International J. of Photoenergy, Vol. 2006 (2006), Article ID 24916, 4 p.

[8] *Meysam Karimi, Mohammad Rabiee, Fathollah Moztarzadeh, Mohammadreza Tahriri, Masoud Bodagh* , Appl. Phys., 2009, Vol. 9, Iss. 6, P. 1263-1268

[10] *Yashar Azizian kalandaragh, M.B. Muradov, R.K. Mammedov, Ali Khodayari,* J. of Crystal Growth, 2007, Vol. 305, Iss.1, P. 175-180

[11] *C.D. Lokhande, B. R. Sankapal, H. M. Pathan, M. Muller, M. Giersig, H. Tributsch*, Appl. Surface Science, 2001, Vol. 181, Iss. 3-4, P. 277-282

[12] *V. Nilima, Hullavarad, Shiva S. Hullavarad*, Photonics and Nanostructures - Fundamentals and Applications, 2007, Vol. 5, Iss.4, P. 156-163

[14] *S.K Panda, S. Chakrabarti, B. Satpati, P.V Satyam, S. Chaudhuri*, J. Physics D: Appl. Phys., 2004, Vol. 37, No 4

[15] *YanDan Wu, LiShi Wang, MingWei Xiao, XinJian Huang*, J. of Non-Crystalline Solids, 2008,Vol. 354, Iss. 26, P. 2993-3000.

[16] *Raghvendra S. Yadav, Priya Mishra, Rupali Mishra, Manvendra Kumar, Avinash C. Pandey*,

[17] Ultrasonics Sonochemistry, 2010, Vol. 17, Iss. 1, P. 116-122.

[18] *Matjaž Kristl, Irena Ban, Anita Dančˇ, Valerija Dančˇ, Miha Drofenik*. Ultrasonics Sonochemistry. 2010, Vol.17, Iss. 5, P. 916-922

[19] *V.P. Singh, R.S. Singh, G.W. Thompson, V. Jayaraman, S. Sanagapalli, V. K. Rangari*, Solar Energy Mat.and Solar Cells, 2004, Vol.81, Iss. 3, P.293-303.

[20] *Hong-liang Li, Ying-chun Zhu, Si-guang Chen, Oleg Palchik, Jin-ping Xiong,*

[21] *Yuri Koltypin, Yosef Gofer, Aharon Gedanken*, J. of Solid State Chemistry, 2003, 172,102–110

[22] *G.Z. Wang, Y. Wang, Y. Zhang, Y. WU, G.H. LI, L. Zhang*, J.Mater.Sci.Techol., 2003, Vol. 19, No.3.

[23] *N. Ghows and M.H. Entezari.* Ultrasonics Sonochemistry, 2011, Vol. 18, Iss. 1, P. 269-275

[24] *Behboudni , B. Khanbabae*, Colloids and Surfaces A: Physicochem. Eng. Aspects 290 (2006) 229–232.

[25] *Azizian Kalandaragh Y., Muradov M.B., Mamedov R.K., Behboudnia M., Khodayari*. J.Opt. adv. mat. (RC), 2008, v. 2, No. 1, p. 42-45

[26] *G.Z.Wang, W.Chen, C.H.Liang, Y.W.Wang, G.W.Meng, L.D.Zhang*, Inorganic Chemistry Communications, 2001, 4 , 208-210.

[27] *M.B. Muradov, Q.M. Eyvazova, N.Q. Darvishov, S.E. Baqirova,* Transactions, ANAS ser. of Phys.-Math. and Tech. Scien.Phys. and Astron., 2004, 24, №.5, 145. (in Russian).

[28] *M.B. Muradov, A.A. Aqasiev.* Pisma v JTF , 1991, 17 ,.13, r. 54. (in Russian).

Received: 21.10.2011

AB INITIO INVESTIGATION OF INFRARED OPTIC PHONON MODES SPLITTING IN TlSe CRYSTAL

V.N. JAFAROVA[1], E.K. KASUMOVA[2], G.S. ORUDZHEV[1, 2]
[1]G.M. Abdullayev Institute of Physics of ANAS
H. Javid ave., 33, AZ-1143, Baku, Azerbaijan
[2]Azerbaijan Technical University
H. Javid ave., 25, AZ-1073, Baku, Azerbaijan

The calculation technique of a splitting of infrared optical phonon frequencies on longitudinal and transverse modes is described. The analysis of splitting at the Brillouin zone center and influence of these splitting on phonon spectrum is carried out on the base of TlSe phonon spectrum derived from ab initio calculations, performed earlier in our papers.

Keywords: TlSe, chain crystal, ab initio calculation, pseudopotential, phonon spectrum, LO-TO splitting
PACS: 534.63

The splitting of phonon frequencies on longitudinal-optic (LO) and transverse-optic (TO) modes is investigated at the Brillouin zone (BZ) center on the base of phonon spectrum obtained from ab initio calculations for tetragonal chain crystal TlSe [1]. The calculation is carried out with norm-conserving relativistic ionic Hartwigsen-Goedecker-Hutter pseudopotentials [2] in local density approximation [3] of density functional perturbation theory [4] using ABINIT program package [5] within the framework of linear response function [6]. Firstly the equilibrium structural and lattice parameters of TlSe crystal are calculated in [7]. The optimization procedure for the definition of structural parameters of crystal equilibrium position is carried out up to force gradient becomes less than 10^{-7} Ha/Bohr. The solving of such type tasks requires the crystal total energy calculations and search of total energy minimum. Kohn-Sham equations [4] are solved and wave functions and electron energy are calculated with this aim by the conjugate gradient minimization method [8] for considered crystal structure. The plane waves with energy not exceeding 20 Ha are used for wave function expansions. The correlation effects are taken into account by Ceperley-Alder-Perdew-Zunger scheme [9]. The BZ integration is carried out using Monkhorst-Pack 2×2×2 k-points grid [10]. Phonon spectrum of TlSe crystal was investigated earlier from model calculations in [11]. The 9 adjustment parameters are introduced and adjustment procedures for 11 experimental optic phonon frequencies defined for BZ center from infrared (IR) lattice reflection (5 frequencies) and Raman (R) spectrum (6 frequencies) in [11] for phonon spectrum calculation with the use of interatomic interaction model accepted by authors. However, some phonon frequencies known from the experiment cannot be identified. The accepted model also does not allow to calculate the LO- and TO splitting of IR-active phonon frequencies at the BZ center and the effect of splitting on the whole spectrum.

The comparable analysis of phonon frequency values calculated from ab initio procedure with the ones obtained from experiments on neutron scattering [12], IR- and R-reflection [13, 14] and from model calculations [11] is given in the [1]. It is revealed that phonon bands of TlSe are divided on two groups by forbidden gap in the frequency region 110÷140 cm^{-1}, and each group is divided on two subgroups with the assumption the picture of phonon density of states. The lowest optic phonon frequency at Γ point of BZ is 16.8 cm^{-1} (exp.: 26 cm^{-1}) with symmetry Γ_9 (A_{2u}), IR-active; and the biggest one is 203.5 cm^{-1} (exp.: 204 cm^{-1}) [14] with symmetry Γ_4 (B_{2g}), R-active. In phonon spectrum of TlSe crystal along K symmetry line connecting the points P and R of BZ the phonon bands are doubly degenerated as a result of symmetry with respect to time reversal. The strong dispersion is observed in the direction of the chains along the symmetric lines D and A in separate branches of the main lower group. The comparably weak dispersion is observed perpendicular to chains for Σ and G symmetry lines. It is revealed that the weak anisotropy is observed in phonon spectrum and values of elastic constants of strongly anisotropic compound TlSe, contrary to expectations [15].

It is known that crystal total energy is related to the macroscopic electric field, $\mathbf{E}_{mac} = E_0 e^{iq\cdot r}$, by the following expression [16]:

$$E(u, E_{mac}) = \frac{1}{2} M\omega_0^2 u^2 - \frac{\Omega}{8\pi} \in_\infty E_{mac}^2 - eZ * u \cdot E_{mac}, \quad (1)$$

here M - mass of considered atom, u - displacement of the atom from its equilibrium position, Ω - the unit cell volume, ε_∞ - dielectric constant, Z* - Born effective charge, e - elementary charge, ω_0 - frequency of the considered mode in the absence of an electric field. The values of the Born effective charge and dielectric constant tensors are calculated in [17].

At presence of intra-crystalline electric field the relative force acting on considered two crystal atoms, is defined by the following expression:

$$F = -\frac{\partial \mathbf{E}}{\partial u} = -M\omega_0^2 u + eZ^* \mathbf{E}_{mac}. \quad (2)$$

The following conditions should be satisfied in the static limit and without activity of external forces:

$$q\times \mathbf{E}_{mac}=0,\ \ q\times D_{mac}=0. \qquad (3)$$

For transverse optic (TO) modes $u_0 \perp q$, i.e. $\mathbf{E}_{mac} = 0$ and relative force is as follows:

$$F=-M\omega_0^2 u\,, \qquad (4)$$

and transverse modes of phonon frequencies are $\omega_{TO} = \omega_0$.

For longitudinal optic (LO) modes $u_0 \parallel q$, i.e. $\boldsymbol{E}_{mac} = 0$, $D_{mac} = 0$ and relative force is:

$$F=-M\left(\omega_0^2+\frac{4\pi e^2 Z^{*2}}{M\Omega\in_\infty}\right)u. \qquad (5)$$

The longitudinal modes of phonon frequencies are expressed as follows:

$$\omega_{LO}=\sqrt{\omega_0^2+\frac{4\pi e^2 Z^{*2}}{M\Omega\in_\infty}}\,. \qquad (6)$$

It is necessary to consider the macroscopic electric field accompanying by collective atomic vibrations at phonon wave vector $q = 0$. In general case, taking into consideration the exact corrections, the matrix of intra-atomic force constants can be expressed as a sum of analytic and non-analytic contributions [16]:

$$\tilde{C}_{k\alpha,k'\beta}(q\to 0)=\tilde{C}_{k\alpha,k'\beta}(q=0)+\tilde{C}^{NA}_{k\alpha,k'\beta}(q\to 0), \qquad (7)$$

Here, depending on the direction, the non-analytic limit is expressed as:

$$\tilde{C}^{NA}_{k\alpha,k'\beta}(q\to 0)=\frac{4\pi}{\Omega_0}\frac{(\sum_\gamma q_\gamma Z^*_{k,\gamma\alpha})(\sum_{\gamma'} q_{\gamma'} Z^*_{k',\gamma'\beta})}{\sum_{\alpha\beta} q_\alpha \in^\infty_{\alpha\beta} q_\beta}, \qquad (8)$$

where Ω_0 is the volume per atom. Note that matrix eigenvectors $\tilde{C}(q\to 0)$ cannot be identified with vectors $\tilde{C}(q=0)$.

Thus, the vibration modes corresponding to phonon frequencies in the direction perpendicular to the wave vector q, split into two parts. The expression that relates LO- and TO-modes is as follows [16]:

$$\omega_m^2(q\to 0)=\omega_m^2(q=0)+\frac{4\pi}{\Omega_0}\cdot\frac{\sum_{\alpha\beta} q_\alpha S_{m,\alpha\beta} q_\beta}{\sum_{\alpha\beta} q_\alpha \in^\infty_{\alpha\beta} q_\beta}. \qquad (9)$$

Here, $S_{m,\alpha\beta}$ is the tensor of mode-oscillator strength and

$$S_{m,\alpha\beta}=\left(\sum_{k\alpha'} Z^*_{k,\alpha\alpha'} U^*_{mq=0}(k\alpha')\right)\times\left(\sum_{k'\beta'} Z^*_{k',\beta\beta'} U_{mq=0}(k'\beta')\right). \qquad (10)$$

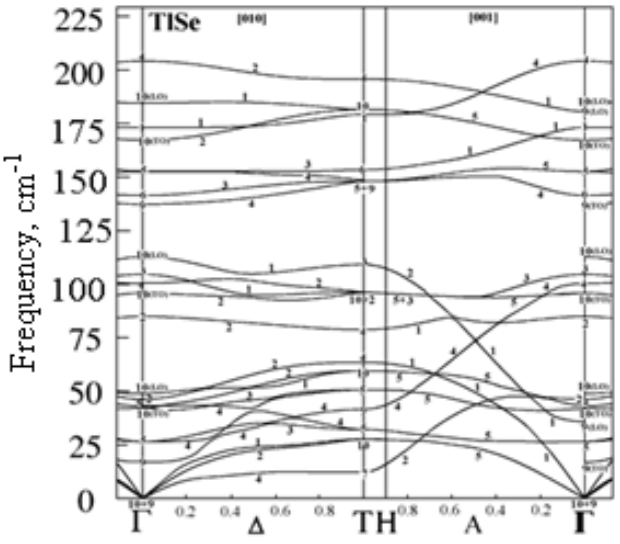

Fig. 1. The TlSe phonon band spectrum calculated for Δ and A symmetry lines and LO-TO splitting at Γ point.

The TlSe phonon band spectrum calculated for Δ and A symmetry lines outgoing from the BZ center, Γ, with taking into account splitting at Γ point IR-active optical phonon frequencies on LO and TO modes, is given in Fig.1. Symmetries of phonon modes in the figure are given in digital form.

IR-active phonon frequencies calculated for TlSe from first principles [1] and defined from experiment [13, 14] are compared and grouped according to symmetries in Table 1. The relative error of the difference between splitted mode-frequencies derived from ab initio calculations and experimental values are given in brackets. The frequency of longitudinal and transverse optical phonon modes in table are separated by slash.

As can be seen, all values are in good agreement with each other. Only for one IR-active mode with symmetry Γ_9 (A_{2u}) the relative error in the calculated and experimental values (calc. 17.6 cm^{-1}; exp. 26 cm^{-1} [14]) is significant (32%). This difference is due to the calculation difficulty of low-frequency optical phonon modes in the ab initio calculations.

Table 1.

The comparison of phonon frequency values obtained from ab initio calculations for TlSe at Γ point with values obtained from experiments on IR- and R-reflection [13,14].

Symmetry of optical phonon modes	LO-TO-splitted phonon frequencies, (cm^{-1})	Experiment	
		[13]	[14]
Γ_9 (A_{2u})	17.6 (32%)/35.3 (3.8%)	26/33IR	26/34IR
	135.8 (0.1%)/177.2 (1%)	136/173IR	134/179IR
Γ_{10} (E_u)	42.1 (6.4%)/48.8 (2.4%)	46 /50IR	45/50IR
	96.1 (9%)/112.6 (4%)	88/103IR	88 /108IR
	166.3 (5%)/183.0 (4.6%)	158/175IR	158/175IR

[1] *G. Orudzhev, V.Jafarova, S.Schorr, K.Mimura, K.Wakita, Y. Shim , N. Mamedov , F. Hashimzade,* Jpn. J. of Appl. Phys. 47, 8193 (2008)

[2] *C. Hartwigsen, S. Goedecker and J. Hutter,* Phys. Rev. B58**,** 3641 (1998)

[3] *W. Kohn and L. Sham,* Phys. Rev. 140, A1133 (1965)

[4] *P. Hohenberg, W. Kohn,* Phys. Rev. 136, B864 (1964)

[5] *X. Gonze, J.M. Beuken, R. Caracas et al.,* Comput. Mater. Sci. 25, 478 (2002)

[6] *S.Baroni, de S.Gironcoli, A.Dal Corso, and P. Giannozzi*, Rev. Mod. Phys. 73, 515 (2001)

[7] *V.N. Jafarova.* Proceedings of ANAS PhD students conference of science (part 1), Baku, 45 (2006) (in Azeri)

[8] *M. Payne, M. Teter, D. Allan, et al.,* Rev. Mod. Phys. 64, 1045 (1992)

[9] *D. Ceperley and B. Alder,* Phys. Rev. Lett. 45, 566 (1980)

[10] *H. Monkhorst and J. Pack,* Phys. Rev. B13, 5188 (1976)

[11] *M.Q. Shaxtaxtinskiy, Dj.A. Quseynov i dr.,* FTP 15, 1522 (1981) (in Russian)

[12] *S.B. Vaxrushev, B.E. Kvyatkovskiy, N.M. Okuneva, K.R. Allaxverdiev i dr.* FTT 26, 1225 (1984) (in Russian)

[13] *N.M .Gasanly, A.S. Ragimov,* Physica B+C 115, 381 (1983)

[14] *K.R. Allakhverdiev, E.A. Vinogradov , N.N. Melnik , M.A. Nizametdinova, et al.,* Phys. Stat. Sol. B87, K115 (1978)

[15] *V.N.Jafarova, G.S.Orudzhev* Selected Works-Fundamental Sciences X(38), 58 (2011) (in Azeri)

[16] *X. Gonze and C. Lee,* Phys. Rev. B55, 10355 (1997)

[17] *V.N. Jafarova, G.S. Orudzhev,* ANAS Transactions XXXII, 18 (2011) (in Azeri)

Received: 12.12.2011

ISSN 1028-8546

2011, Vol. XVII, 4
Section: En

CONTENTS

NOTES

NOTES

NOTES